



Hydraulic Fracture Vertical Propagation Mechanism in Interlayered Brittle Shale Formations: An Experimental Investigation

Jun Zhang¹ · Qiangang Yu¹ · Yuwei Li² · Zhejun Pan¹ · Bo Liu¹

Received: 19 July 2022 / Accepted: 21 September 2022 / Published online: 6 October 2022
© The Author(s), under exclusive licence to Springer-Verlag GmbH Austria, part of Springer Nature 2022

Abstract

To investigate the vertical propagation mechanism of hydraulic fractures in interlayered brittle shale formations in the Qingyi member of the Southern Songliao Basin in Northeast China, an experimental model for simulating the shale within thin sandstone interlayers is designed. This model reflects the relative difference of the mechanical properties and brittleness characteristics between shale and sandstone. When combining a series of true triaxial hydraulic fracturing experiments with fracture area measurement, three-dimensional fracture reconstruction, and acoustic emission (AE) monitoring, the effects of the key geological and engineering factors on the fracture vertical propagation behaviors in interlayered shale formations are quantitatively studied. The experimental results showed four types of hydraulic fracture propagation patterns in interlayered shale formation: *arresting pattern*, *deflecting pattern*, *penetrating pattern* and *composite pattern*. The interlayer dip angle is negatively correlated with the penetrating ability of the hydraulic fracture, while the vertical in situ stress difference and interface cementation strength are positively correlated with the penetrating ability of the hydraulic fracture. The brittleness characteristics of the interlayer have a considerable effect on the propagation behavior of the hydraulic fracture. The interlayer with weak brittleness inhibits the hydraulic fractures' ability to penetrate the interfaces and interlayers owing to the plastic deformation of the interlayer, thereby consuming considerably more elastic energy that should have been applied to fracture propagation. Under a higher injection rate and viscosity, the infiltration of the fracturing fluid in the interface is less, the hydraulic energy accumulated at the fracture tip is more concentrated, and the hydraulic fracture's ability to penetrate through the interface into the interlayer is strengthened. The results of this study can provide a deeper understanding of fracture geometry and the fracture intersection mechanism in the continental interlayered shale formation, providing a more accurate guidance for fracturing parameter optimization.

Highlights

- Communicate multiple shale oil formations through one fracturing operation.
- Model is used to analyze the vertical propagation of fractures in multi-lithologic formation.
- Results show the influence of interlayer brittleness on hydraulic fracture propagation.
- Hydraulic fracturing effect can be improved by controlling injection rate and viscosity of fracturing fluid.

Keywords Interlayered shale formation · Fracture propagation · Shale and sandstone brittleness · Penetrating interface · Interaction behavior

List of Symbols

HFE	Hydraulic fracturing experiment
BFZ	Bedding fracture zone
AE	Acoustic emission
HIS	High-strength interface
LSI	Low-strength interface
PSL	Plastic sandstone interlayer
BSL	Brittle sandstone interlayer
B	Dip angle of interlayers

✉ Yuwei Li
liyuweibox@126.com

¹ Department of Petroleum Engineering, Northeast Petroleum University, Daqing 163318, China

² School of Environment, Liaoning University, Shenyang 110036, China

$\Delta\sigma_{vh}$	Vertical stress difference
Q	Injection rate
η	Fracturing fluid viscosity
FPZ	Fracture process zone
U①, U②	Two interlayer interfaces at the upper end of the sample
L①, L②	Two interlayer interfaces at the lower end of the sample
B	Brittleness index
E	Elastic modulus after positive normalization of logging data
μ	Poisson's ratio after inverse normalization of logging data

1 Introduction

The Qingyi member of the Southern Songliao Basin in Northeast China is rich in continental sedimentary shale oil resources and has great development potential. In some areas, the Qingyi member contains multiple sets of pay zones with uneven thicknesses and is vertically separated by thin sandstone interlayers (Liu et al. 2017; Li et al. 2017; Liu et al. 2019a, b; Zhang et al. 2020a; Luo et al. 2021; Cong et al. (2022a, b)). Owing to the weak structural planes in this type of well-developed interlayered shale formations, the height of the hydraulic fractures is challenging to control. Further, the development approach of separate-layer fracturing reduces the shale oil production (Guo et al. 2016; Zheng et al. 2019; Lu et al. 2020; Xie et al. 2020). To improve the efficiency of hydraulic fracturing and shale oil resource development, oilfield engineers hope to make the hydraulic fractures penetrate through the sandstone interlayers and communicate with multiple shale oil pay zones during the implementation of the hydraulic fracturing project. Therefore, it is critical to understand the propagation mechanism of hydraulic fractures in the interlayered shale formation and realize the primary factors affecting the ability of hydraulic fractures to penetrate the interlayers (Gao et al. 2018; Li et al. 2019, 2020a; Wang et al. 2021).

The actual geometry and morphology of the hydraulic fractures in the reservoir cannot be directly observed; thus, the hydraulic fracturing experiment (HFE) is utilized as the primary approach to investigate the propagation mechanism of hydraulic fractures (Fraser-Harris et al. 2020; Zhuang et al. 2020; Inskip et al. 2020). Shale is a typical layered rock mass, which is generally used to study the complex propagation behaviors of hydraulic fractures (Zhou et al. 2018; Wan et al. 2018; Chong et al. 2019; Wu et al. 2019). Guo et al. (2014) conducted the HFEs under true triaxial stress conditions using the layered shale outcrop. They observed the fracture initiation and extension morphology via the fault computerized tomography scanning technology.

Tan et al. (2017) studied the fracture initiation and vertical propagation behaviors in layered shale using HFEs; they divided the hydraulic fracture extension mode into four categories: single fracture, fishbone fracture, fishbone fracture with fracture opening, and multilateral fishbone fracture network. Zou et al. (2017) explored the density and permeability effects of bedding planes on the penetration behavior of hydraulic fractures in shale using the HFEs. However, due to the randomness and heterogeneity of the bedding planes' distribution in natural shale, the dispersion of the HFE results is usually large. Therefore, some scholars used artificial layered samples to study the fracture propagation behaviors (Daneshy 1978; Wang et al. 2016). Sarmadivaleh and Rasouli (2015), Fu et al. (2016), Zhao et al. (2016), Tan et al. (2018) and Aimene et al. (2019) used cement mortar to prepare the layered rock mass and investigated the influence of the interbed material mechanical properties and interface cementation strength on the fracture propagation behavior through a series of true triaxial HFEs. Their unified understanding is as follows: (1) the interlayer with a large thickness and high strength will reduce the penetration ability of the hydraulic fractures, easily producing branch cracks along the weak interface between the layers and (2) the interface with an incomplete or a low cementation strength can significantly inhibit the propagation of the fracture height. Ella Mari'a Llanos et al. (2017) studied the effects of the friction characteristics of the interlayer interface on the hydraulic fracture's ability to penetrate using the cementless multi-layer sandstone model. They found that when the friction resistance of the interface is large, the hydraulic fracture will penetrate the interlayer, irrespective of whether the interlayer interface is cemented. Huang and Liu (2017) used concrete to prepare the interbedded fracturing samples, comprising a three-layered structure, and studied the interaction between the hydraulic fractures and interlayer interfaces. Their results showed three propagation patterns of the hydraulic fractures when encountering interfaces with different cementation strengths or under different stress conditions: deflecting along the interface, offsetting along the interface and subsequently repenetrating it, and directly penetrating the interface. Subsequently, Zhang et al. (2021b), Zhang et al. (2021a) performed a theoretical analysis of the experimental results of Huang and Liu (2017). They proposed that the interface between the layers had been damaged, forming a bedding fracture zone (BFZ) under the action of stress disturbance around the hydraulic fracture before it intersected with the hydraulic fracture. The in situ stress differences and interface cementation strengths are the internal factors affecting the hydraulic fractures' penetration ability, whereas the fluid injection rate and viscosity are the external factors.

The above research is aimed at the single lithologic layered formation. Currently, there are few experimental studies on the fracture propagation mechanism of multilithologic

superimposed formations (Athavale and Miskimins 2008; Roundtree and Miskimins 2016; Xu et al. 2015). El (1987) found that hydraulic fractures require a higher in situ stress difference to penetrate the interface from rocks with a lower elastic modulus to rocks with a higher elastic modulus. Casas et al. (2006) studied the effects of in situ stress difference, fracturing fluid viscosity, and lithology difference on hydraulic fracture propagation using the heterogeneous rock model prepared with cement and sandstone. Their results showed that the high-stress difference and high-viscosity fracturing fluid promote the fracture to penetrate through the interface, while the elastic modulus difference of the layers has little effect on the fracture propagation behavior. Li et al. (2014), Tan et al. (2019, 2021), Cao et al. (2020), conducted a series of HFEs using natural coal–rock composite samples. They found that the conditions of low interlayers' stress difference, elastic modulus difference, and permeability difference as well as high pumping rate can increase the possibility of the hydraulic fracture penetrating the interlayer interface.

Some results have been obtained on the fracture propagation mechanism in sandstone–shale interlayered formation through the numerical method; however, there are relatively few experimental studies (Zhao et al. 2018; Li et al. 2020b, 2021; Ju et al. 2019; Cheng et al. 2022; Song et al. 2022). In addition, an important parameter for predicting the hydraulic fracturing effect is the influence of rock brittleness on fracture propagation, which has not been studied yet. Herein, the physical and mechanical parameters of the sandstone and shale layers of the Qingyi interlayered shale oil formation in the Songliao Basin were measured via laboratory mechanical tests. Next, an experimental model for simulating the sandstone–shale interlayered formation was designed using similar materials that can reflect the relative differences of the mechanical properties and brittleness characteristics between sandstone and shale. Finally, the vertical fracture propagation mechanism in the interlayered formation was studied using a series of HFEs in combination with acoustic emission (AE) monitoring technology.

2 Characteristics of the Sandstone–Shale Interlayered Formation

2.1 Physical Properties

The logging data and core observations show that the shale oil formation of the Qingyi member longitudinally includes three types of lithology: shale, mudstone, and thin sandstone. The lithology combination can be further divided into three types: a large set of pure, hugely thick shale; mudstone–shale interbed; and sandstone–shale interlayer (Fig. 1). Shale intercalated with the thin sandstone interlayers is the main

research object of this study, which contains 59% brittle minerals and has a good hydraulic fracturing potential. The thickness of the sandstone interlayer is between 0.2 and 5.8 m, the average thickness is 1.6 m, and the interlayer weak structural planes are very well developed. The test data show that the effective porosity and gas permeability of the dry shale sample are 5.1% and $0.15 \times 10^{-3} \mu\text{m}^2$ respectively, and the effective porosity and gas permeability of dry sandstone sample are 10.6% and $3.49 \times 10^{-3} \mu\text{m}^2$, respectively.

2.2 Mechanical Properties

To obtain the mechanical parameters of sandstone and shale, the Brazilian splitting test and triaxial compressive test were performed and the test results are shown in Table 1 and Fig. 2. According to the test results, the following formula is used to calculate the brittleness index of shale and sandstone: $B = 0.5 \times (E + \mu)$, where E and μ represent the elastic modulus and Poisson's ratio of rock, respectively. The tensile strength and compressive strength under various confining pressures of sandstone are higher than those of shale. Conversely, when compared with shale, the elastic modulus of sandstone is smaller, and the Poisson's ratio is larger, which indicates that the brittleness index of shale is considerably higher than that of sandstone. Rock brittleness is closely related to its fracture characteristics. Brittleness can reflect the ability of rock to sustain macro failure after energy accumulation and release under specific conditions. The more brittle the rock, the more likely it is to have multiple fracture modes. The results of our tests also confirm this rule (Ai et al. 2016; Tang et al. 2019, 2021; Xie et al. 2020; Zhao et al. 2022). In Fig. 2, under the same load conditions, the sandstone sample shows a single shear failure pattern, whereas the shale sample shows a complex failure pattern with multiple longitudinal cracks. The failure pattern of shale is due to the efficient accumulation and full release of elastic energy, which is a typical feature of brittle rupture, indicating that the hydraulic fractures are easier to extend in the shale formation.

3 Hydraulic Fracturing Experiment of Sandstone–Shale Formation

3.1 Preparation Method of the Experimental Model for Simulating the Sandstone–Shale Interlayer

It is challenging to conduct HFE with full diameter cores extracted from the underground because most cores have dense fractures resulting from the influence of stress release. Therefore, artificial samples are used for HFE in this paper. Artificial rock samples have been used in hydraulic fracturing tests by many scholars (Zhang et al. 2017, 2019;

Fig. 1 Logging curve and lithology combination characteristics (2410–2420 m in the Qingyi member)

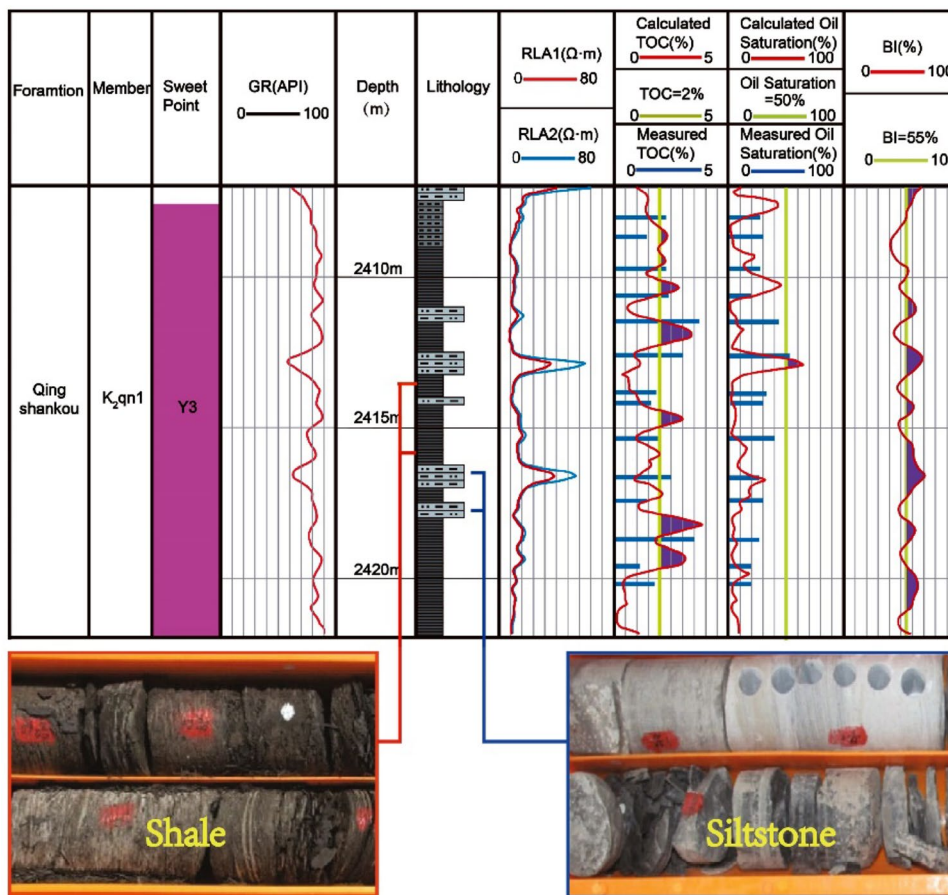


Table 1 Mechanical parameters of shale and sandstone

Type	Tensile strength (MPa)	Confining pressure (MPa)	Compressive strength (MPa)	Young's modulus (GPa)	Poisson's ratio	Brittleness ($B = \frac{E+\mu}{2}$)
Shale	4.59	0	61.22	25.23	0.18	0.64
		15	77.15	22.17	0.19	0.56
		30	103.37	26.25	0.23	0.57
Sandstone	6.49	0	84.92	13.25	0.24	0.29
		15	121.51	16.85	0.25	0.34
		30	138.41	18.25	0.26	0.35

The bold values are used to highlight differences from other parameters

Cong et al. 2022a, b; Xue et al. 2022). The advantage of artificial rock sample is that the sample structure can be changed according to the experiment purpose, and the weak surface can be preset according to a certain angle and number, so as to obtain quantitative test results and rules. However, how to obtain similar materials with mechanical properties similar to those of natural rocks is a difficult problem for artificial samples. An experimental model for simulating the sandstone–shale interlayered formation is designed herein. As shown in Fig. 3, this model has a size of 300 × 300 × 300 mm, including four sandstone layers and

three shale layers. An injection pipe simulating the horizontal well is present in the middle shale layer, which has a spiral perforation with a perforation depth of 10 mm and a phase angle of 60°.

The key challenge herein is making the mechanical properties of the experimental model close to those of the real sandstone–shale interlayered formation. The test results in Sect. 3 show that there are two significant differences in the mechanical properties between sandstone and shale. The first is that the strength of sandstone is significantly higher than that of shale. To reflect the strength difference of

Fig. 2 Mechanical test results of shale and sandstone

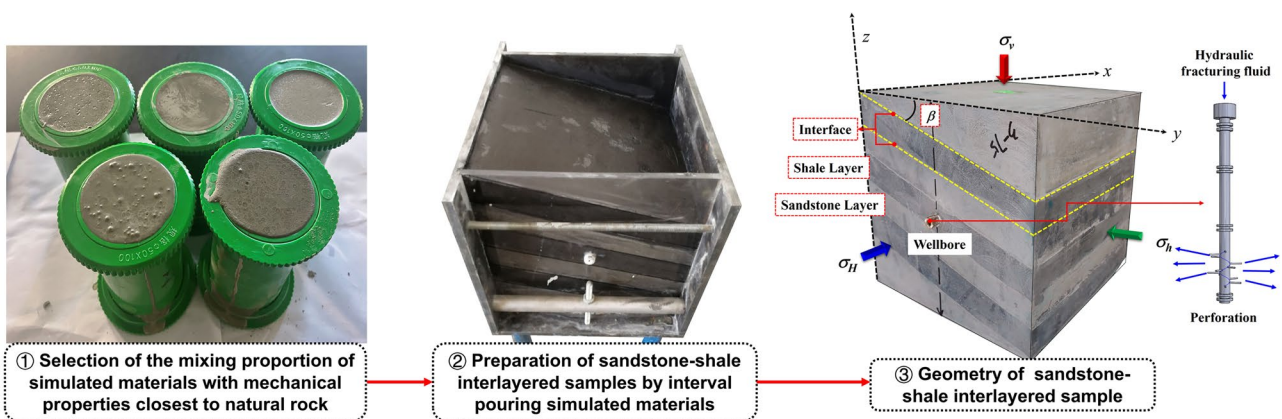
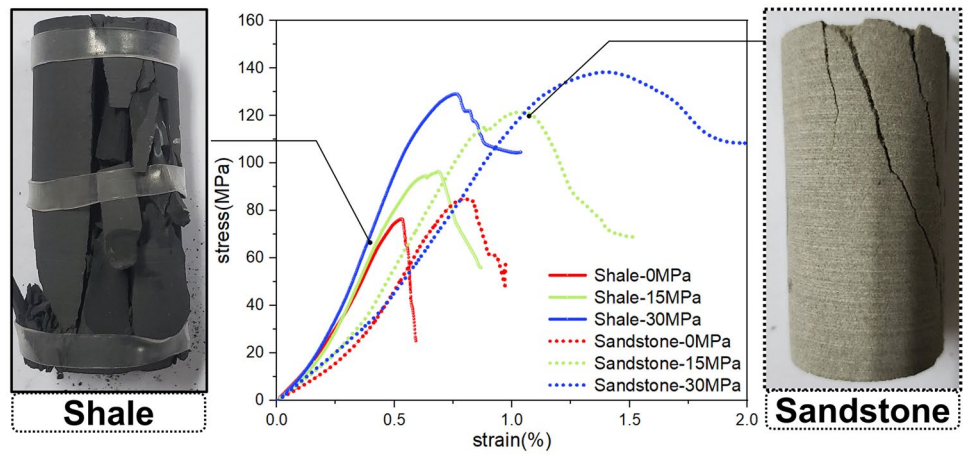


Fig. 3 Preparation process and geometric structure of the experimental model for simulating the sandstone–shale interlayered formation

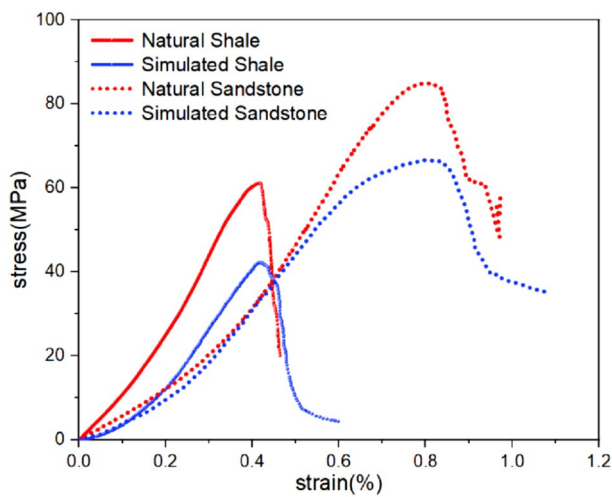
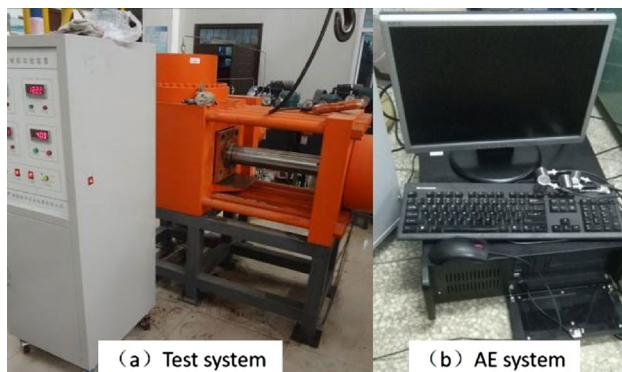
the simulated material, 62.5 high-strength portland cement and 42.5 ordinary portland cement were used as cementing agents for sandstone and shale, respectively. The high-purity quartz sand (particle size range 0.075–0.109 mm) was used as filling material. The second difference is that the elastic modulus and brittleness of shale are considerably higher than the elastic modulus and brittleness of sandstone. To increase the elastic modulus of the shale-simulated material, a certain proportion of silicon powder was added to the formula. To increase the ductility of the sandstone-simulated material, kaolinite powder was added to reduce the elastic modulus and a superplasticizer was added to maintain the strength. Herein, the simulated materials with mechanical properties closest to natural sandstone and shale are selected using mechanical experiments from 50 proportioning schemes. Table 2 and Fig. 4 show the comparison of the mechanical properties between natural rocks and simulated materials. Although the simulated materials have some mechanical differences compared to the natural samples, they can reflect the relative differences in the mechanical properties between

sandstone and shale. This paper focuses on the influence of the interface cementation strength, stress state and brittleness of shale and sandstone formation on the longitudinal propagation of hydraulic fractures, so the anisotropy of shale caused by bedding is not considered.

As shown in Fig. 3, the mortar of the simulated materials mixed by a mud mixer is slowly poured into the cube mold. The mold has a transparent plexiglass on one side where the position of the interface is marked. The mixed material for one rock layer is poured and solidified for 2 h before pouring the next rock layer. The strength change of the interface must be considered in the experiment, and it can be adjusted by changing the pouring interval of each rock layer. When the experimental model containing seven rock layers has been poured and is ready for drying, it must be cured in a standard curing box (temperature at 20 °C, humidity > 95%) for 28 days.

Table 2 Mechanical parameters and the final mixing ratio of shale- and sandstone-simulated materials

Rock Type	Tensile strength (MPa)	Compressive strength (MPa)	Young's modulus (GPa)	Poisson's ratio	Brittleness ($B = \frac{E+v}{2}$)	Mixture ratios (mass)
Natural shale	3.12	61.22	25.23	0.18	0.64	–
Simulated shale material	2.01	42.54	25.46	0.23	0.55	42.5 cement:quartz sand:water:silica fume:iron powder = 1.00:0.80:0.35:0.15:0.25
Natural sandstone	5.85	84.92	13.25	0.24	0.29	–
Simulated sandstone material A	4.44	66.89	15.12	0.27	0.26	62.5 cement:quartz sand:water:kaolin:water reducer = 1.00:1.40:0.65:0.15:0.015
Simulated sandstone material B (brittle)	3.24	67.85	24.58	0.23	0.53	62.5 cement:quartz sand:water = 1.00:0.80:0.55

**Fig. 4** Stress–strain curves of the natural and simulated samples**Fig. 5** Hydraulic fracturing physical simulation test system and AE monitoring system

3.2 Experimental Equipment and Scheme

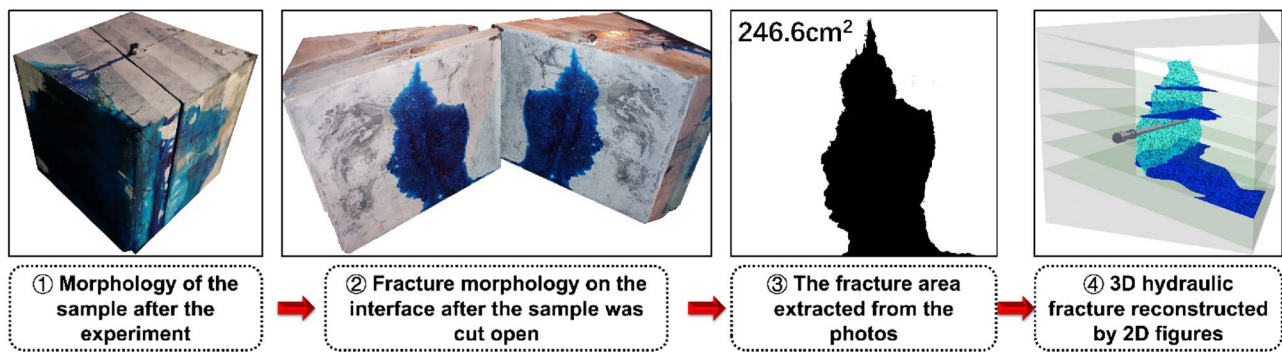
The true triaxial hydraulic fracturing physical simulation experiment system is adopted to implement the HFEs herein (Fig. 5); this system can independently load the test sample in three directions to simulate the in situ stress in the formation. A PCI-2 AE system is used to monitor the fracture initiation and propagation in the samples. Eight AE sensors are installed in the grooves of the loading plates. During the hydraulic fracturing process, the data acquisition system automatically monitors and records the injection rate, pressure, and AE signal.

The scheme of HFE is shown in Table 3. The cementation strength of the interfaces in the sample can be controlled by the manufacturing time interval of each rock layer, and the interlayer brittleness can be adjusted by changing the simulated material (Table 2). Additionally, herein, the interfacial cementation strength of the adjacent rock layers at different manufacturing intervals is tested. When the manufacturing intervals of each layer are timed at 2 and 6 h from onset of material mixing, the cementation strength of the interfaces are measured and are 1.72 and 0.71 MPa, respectively. To facilitate the analysis, high-strength and low-strength interfaces are defined as HSI and LSI, respectively. The plastic and brittle sandstone interlayers (PSL and BSL) are composed of simulated sandstone materials A and B, respectively. In the experimental scheme, M15-0 is used as the reference sample for comparison with the other experimental groups. The sample M15-0 contains PSL and LSI with a dip angle (β) of 15° ; it is tested under the following conditions. The maximum horizontal principal stress (σ_H) is 23 MPa, the minimum horizontal principal stress (σ_h) is 20 MPa, the vertical in situ stress (σ_v) is 26 MPa, the vertical stress difference ($\Delta\sigma_{vh}$) is 6 MPa, the injection rate (Q) is 20 mL/min and the fracturing fluid viscosity (η) is 1 mPa s.

Figure 6 shows the morphology of the sample after HFE processing. It is challenging to analyze and determine the

Table 3 Experimental scheme of the true triaxial hydraulic fracturing experiments (HFEs)

Group	Number	β ($^{\circ}$)	σ_v (MPa)	$\Delta\sigma_{vh}$ (MPa)	Brittleness of interlayer	Strength of interface	Q (mL/min)	η (mPa s)
Reference sample	M15-0	15	26	6	Plastic	High	20	1
Change in interlayer dip angle	M0-0	0	26	6	Plastic	High	20	1
	M30-0	30	26	6	Plastic	High	20	1
Change in vertical stress difference	M15-1	15	29	9	Plastic	High	20	1
Change in brittleness of interlayer	M15-2	15	29	6	Brittle	High	20	1
Change in interface strength	M15-3	15	26	6	Plastic	Low	20	1
Change in injection rate	M15-4	15	26	6	Plastic	High	10	1
Change in fluid viscosity	M15-5	15	26	6	Plastic	High	20	25

**Fig. 6** Hydraulic fracturing experiment (HFE) processing procedure of the samples

internal fracture shape only from appearance, since the blue fracturing fluid is only filtered out from some interfaces. To obtain more intuitive fracture geometry, the sample is cut along the interface to observe and analyze the internal fractures. The fracture shape on each interface is extracted using Photoshop. Next, the hydraulic fracture area is calculated, and the three-dimensional fracture morphology is reconstructed.

4 Fracture Propagation Pattern in the Sandstone–Shale Interlayered Formation

A fracture process zone (FPZ) is present at the tip of the dynamically extended hydraulic fracture, where stress concentration effects, including significant tensile and shear stresses, are observed (Blanton 1986; Renshaw and Pollard 1995; Zhang et al. 2020b, 2021b). Three types of microcracks may appear in the FPZ before the hydraulic fracture intersects with the interface, which can dominate the subsequent fracture propagation behavior (Fig. 7a). Crack A is defined as a tensile microcrack in the sandstone layer caused

by the tensile stress in FPZ in the fracture height direction, exceeding the tensile strength of sandstone. Crack B is defined as a shear microcrack on the interface caused by the shear stress in FPZ in the fracture height direction, exceeding the shear strength of the interface. Crack C is defined as a tensile microcrack in the shale layer caused by the tensile stress in FPZ in the fracture length direction, exceeding the tensile strength of shale.

Under the induction of these three types of microcracks, there may be four propagation patterns of hydraulic fractures in the interlayered formation (Fig. 7b). *I-arresting pattern*: the stress in FPZ in σ_v direction can neither produce Crack A nor Crack B. Only Crack C forms at the fracture tip in shale layer. Subsequently, the hydraulic fracture can only propagate along σ_H direction, which is like a typical Perkins–Kern–Nordgren (PKN) fracture. *II-deflecting pattern*: the sandstone remains stable; however, Crack B forms on the interface in FPZ in σ_v direction under the action of stress induction. Subsequently, the hydraulic fracture deflects and extends along the interface. At the same time, Crack C forming near the fracture tip in shale layer forces the hydraulic fracture to propagate in the fracture length direction. *III-penetrating pattern*: Crack A appears in the sandstone in σ_v direction but the interface remains stable, and Crack C

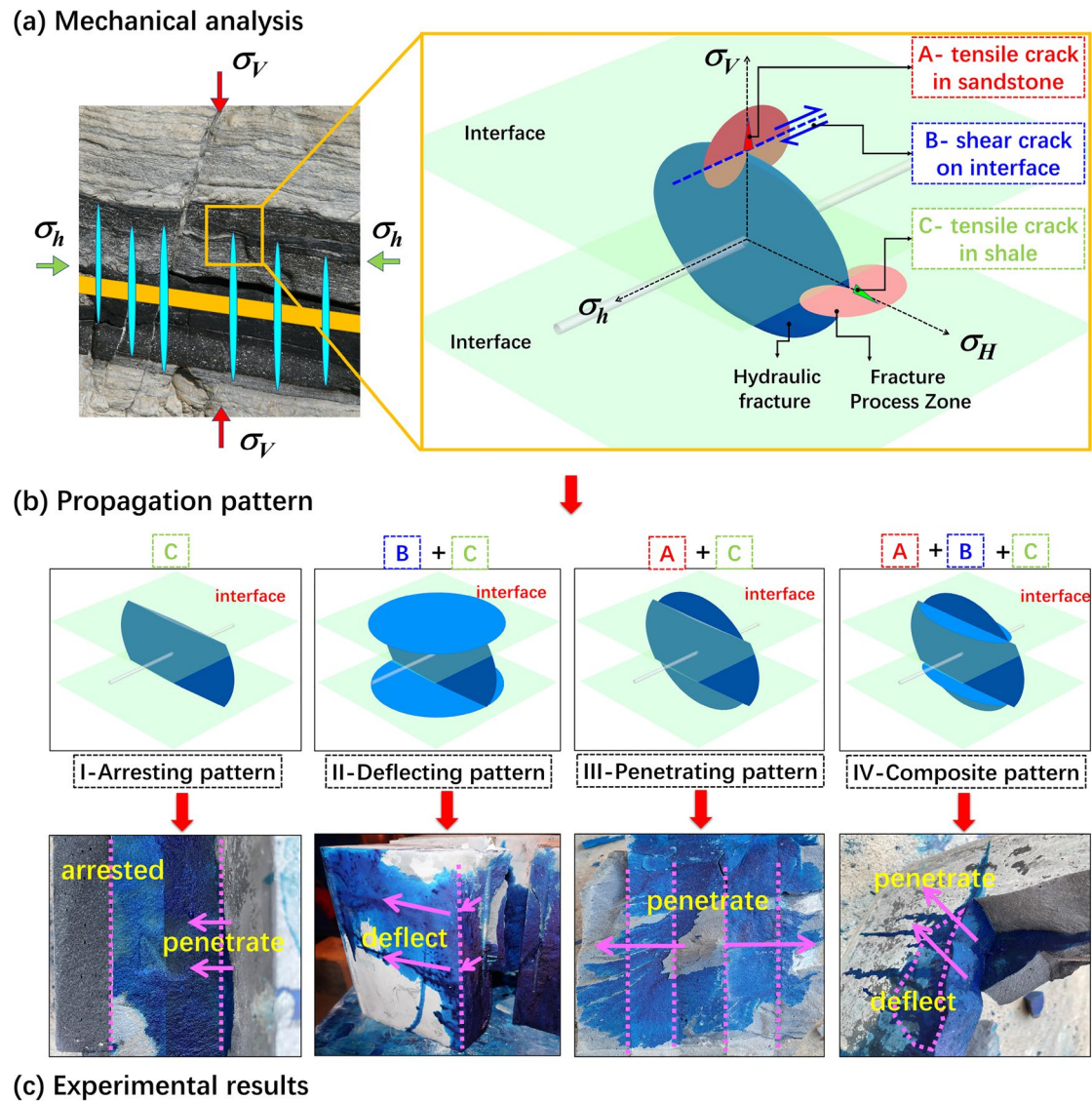


Fig. 7 Propagation patterns of hydraulic fractures in the interlayered samples

appears in σ_H direction. Currently, the hydraulic fracture penetrates the interface into the sandstone layer as well as propagates into the shale layer to maintain the fracture length. IV *composite pattern*: the conditions for forming Cracks A, B, and C are met simultaneously. The hydraulic fracture shows a composite propagation pattern of penetrating the interface and enters the sandstone layer, deflecting along the interface and propagating into shale layer in σ_H direction.

Additionally, the experiments herein show the above four propagation patterns (Fig. 7c). Only when the mechanical properties of the sandstone interlayer and interface are highly stable, the hydraulic fracture can propagate in the σ_H direction in the shale layer without penetrating and deflecting along the interface. Therefore, the

occurrence of the *arresting pattern* is rare in experimental results. When considering the *deflecting pattern*, the hydraulic fracture propagates along one side of the interface, and a large amount of fracturing fluid is filtered into it. In Fig. 7c, the fracture propagation along the interface is nonuniform due to the nonuniformity of the mechanical properties of the interface. The *penetrating pattern* represents that there is no shear instability at the interface as the hydraulic fracture penetrates it. Notably, a small amount of fracturing fluid is still filtered into the interfaces at the intersection point when the hydraulic fracture penetrates them in the experimental results of this study. The reason for this phenomenon is that the interfacial permeability is higher than that of the rock matrix. Even when there is no shear instability at the interface, a small part of the

fracturing fluid will leak into the interface at the intersection point, affording a small range of tensile failure at the interface's intersection point with further extension of the penetrated fracture and an increase of fluid pressure in the fracture.

5 Influence of the Geological Conditions on Fracture Propagation Behavior in the Sandstone–Shale Interlayered Formation

This section primarily studies the influence of the formation conditions, such as the interlayer dip angle, vertical in situ stress difference, interface strength, and interlayer brittleness on fracture propagation behavior.

5.1 Influence of the Interlayer Dip Angle

In Fig. 8a, when $\beta = 15^\circ$, the propagation pattern of the hydraulic fracture is very complex. To facilitate the analysis, this study defines the upper two interfaces and the lower two interfaces encountered by hydraulic fractures as U① and U② and L① and L②, respectively. In the reference sample M15-0, the hydraulic fracture penetrates the interfaces U① and U② and L①; however, only U① has a larger range of fracturing fluid seepage due to the interface opening. Therefore, the hydraulic fracture has the *penetrating patterned* interaction with U② and L① and *composite patterned* interaction with U①. Subsequently, the hydraulic fracture propagation pattern changes from the *penetrating*

pattern to the *deflecting pattern* when the hydraulic fracture encounters the interface L②. Therefore, the hydraulic fracture propagation pattern in the reference sample M15-0 is a II–III–IV composite. Figure 8b shows the injection pressure and the AE curve of M15-0. The hydraulic fracture initiation pressure is 19.15 MPa, and the injection pressure in the propagation stage fluctuates alternately in large and small amplitudes, which reflects the alternating transformation of the hydraulic fractures propagating along the interface and in the rock matrix. In the second rising stage of the injection pressure (489–543 s), the AE energy is significant, which is the characteristic of the rock matrix refracturing after the hydraulic fracture encounters the interface. When $t = 823$ s, the injection pressure decreases greatly and subsequently maintains a low propagation pressure, which corresponds to the propagation behavior of the hydraulic fracture deflection along interface L②. The AE energy in this stage is low, which shows that the AE signal is weak when the hydraulic fracture expands in the interface.

Figures 9a and 10a show the HFE results of sample M0-0 ($\beta = 0^\circ$) and M30-0 ($\beta = 30^\circ$), respectively. When compared to the reference sample M15-0, the fracture propagation patterns of M0-0 and M30-0 are relatively simple. The interactions between the hydraulic fracture and each interface in M0-0 represent a *penetrating pattern*. There is only a very small range of the fracturing fluid infiltration on each interface. When considering the fracture propagation pattern of M30-0, the hydraulic fracture propagation is mainly dominated by the *deflecting pattern*, which deflects and expands along the interfaces U① and L①. In Figs. 9b and 10b, the fracture initiation pressures of M0-0 and M30-0 are 18.23 and 19.54 MPa, respectively, which are different

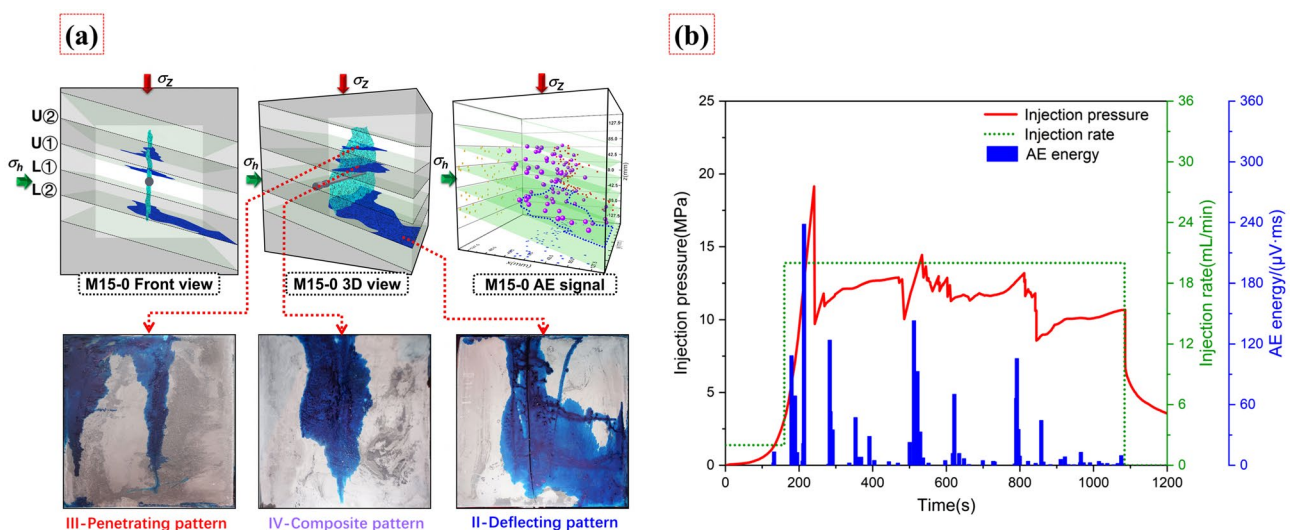


Fig. 8 HFE results of the sample when $\beta = 15^\circ$ (reference sample M15-0): a hydraulic fracture propagation pattern; b injection pressure curve and AE curve

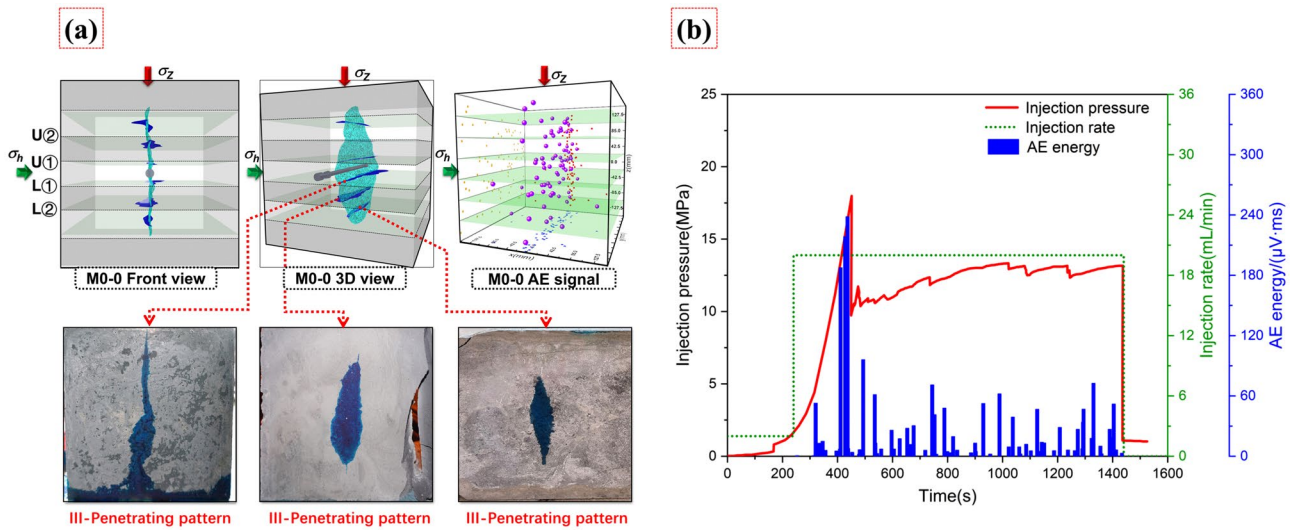


Fig. 9 HFE results of the sample when $\beta=0^\circ$ (M0-0): **a** hydraulic fracture propagation pattern; **b** injection pressure curve and AE curve

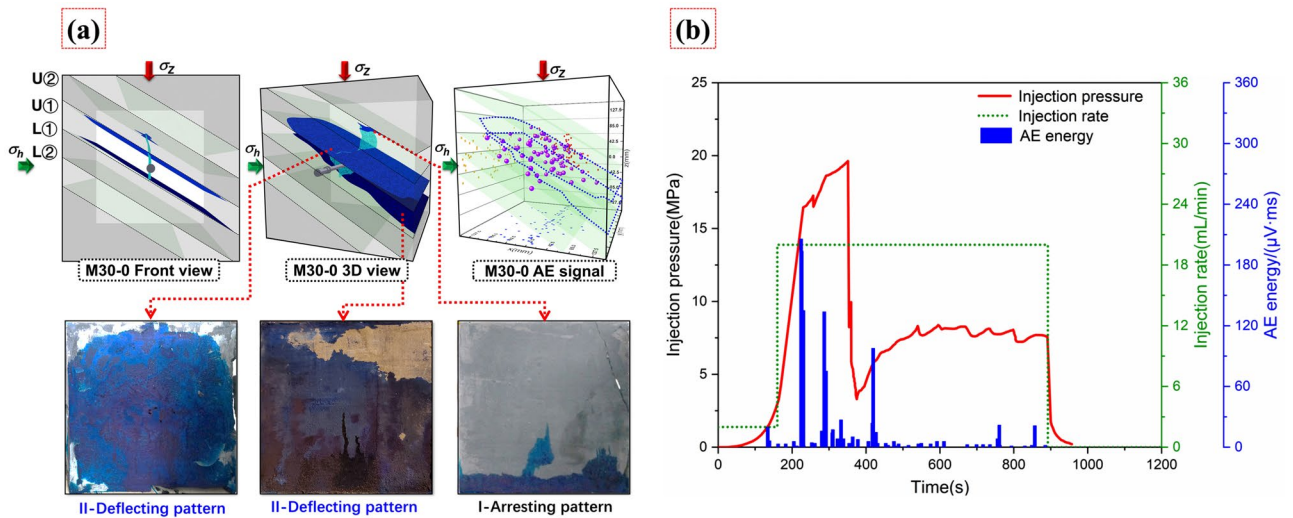


Fig. 10 HFE results of the sample when $\beta=30^\circ$ (sample M30-0): **a** hydraulic fracture propagation pattern; **b** injection pressure curve and AE curve

from that of M15-0, indicating that the interlayer dip angle has little effect on the fracture initiation pressure. In addition, there is a small fluctuation in the propagation stage of the injection pressure curve of M0-0, and the AE energy distribution is relatively dispersed; this result is characteristic of the stable extension of hydraulic fractures in the rock matrix. The injection pressure curve of M30-0 significantly decreased after reaching the fracture pressure and remained at a relatively small value to maintain the fracture propagation. The AE energy of the hydraulic fracture deflecting along the interfaces U $\textcircled{1}$ and L $\textcircled{1}$ is small. Notably, a small crack re-penetrated on the interface U $\textcircled{0}$, indicating an initial microcrack at the edge of interface U $\textcircled{0}$; this result may be

caused by the instability of the initial confining pressure upon loading.

Figure 11 shows the comparison of the cumulative AE energy of the samples with different interlayer dip angles. The cumulative AE energy curves of the three samples increase rapidly and greatly in the fracture initiation stage, but are different in the fracture propagation stage. The cumulative AE growth of sample M0-0 ($\beta=0^\circ$) is relatively stable, which reflects the stable propagation pattern of the hydraulic fractures in rock matrix. The cumulative AE energy of sample M30-0 ($\beta=30^\circ$) increases slightly, and the curve is very flat, which reflects the fracture propagation along the interface. The cumulative AE energy curve of the

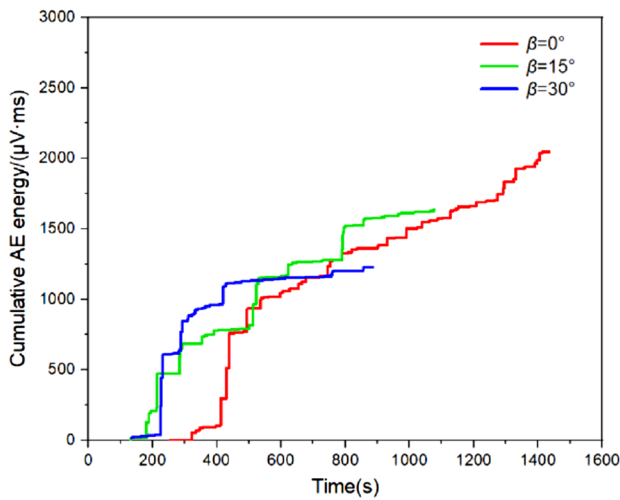


Fig. 11 Cumulative AE energy of samples with different dip angles

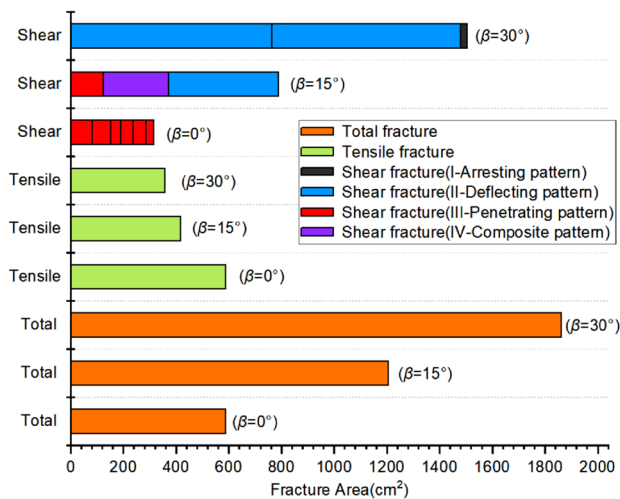


Fig. 12 Statistics of hydraulic fracture area of samples with different dip angles

reference sample M15-0 ($\beta = 15^\circ$) shows a step-by-step rise with alternating slow and sharp increases, which reflects the mutual transformation of the interface opening and matrix refracturing.

Figure 12 shows the quantitative statistics of the hydraulic fracture areas. Herein, the fractures propagating in the rock matrix and deflecting along the interface are defined as tensile fractures and shear fractures, respectively. Two changes are observed as the dip angle of the interlayer increases from 0 to 30° . Conversely, the total area of the hydraulic fractures increases by 1276.2 cm^2 ; the tensile fractures' area decreases by 228.6 cm^2 , and the shear fractures' area increases by 1189.1 cm^2 . Conversely,

the interaction between the hydraulic fracture and interface gradually changes from the *penetrating pattern* to the *composite pattern* and subsequently to the *deflecting pattern*. This result shows that the increase of the interlayer dip angle increases the propagation range of the hydraulic fractures, inhibiting the penetration behavior of the hydraulic fractures. To communicate multiple shale formations during one fracturing operation, selecting the interlayered formation with a small dip angle is required.

5.2 Influence of Vertical In Situ Stress Difference

Figure 13 shows the HFE results of M15-1 ($\Delta\sigma_{vh} = 9 \text{ MPa}$). When compared with the reference sample M15-0 ($\Delta\sigma_{vh} = 6 \text{ MPa}$), the interaction between the hydraulic fracture and interface of sample M15-1 is dominated by the *penetrating pattern*, as shown in Fig. 13a. In Fig. 13b, the fracture initiation pressure of M15-1 is 20.48 MPa , which is close to that of reference sample M15-0. Herein, the vertical in situ stress difference is increased by maintaining the horizontal minimum principal stress and gradually changing the vertical stress; the vertical stress difference has little effect on fracture initiation. The propagation stage of the injection pressure curve of sample M15-1 fluctuates slightly; there is only one significant decrease with an increase only around 500 s . Combined with the characteristics of a small amount of AE energy at this time, it can be determined that there is a *composite patterned* interaction between the hydraulic fracture and at least one of the interfaces. Because a certain range of fracturing fluid is filtered in the interface L $\textcircled{1}$ near the intersection point, it can be considered that the hydraulic fracture exhibits *composite pattern* when it encounters L $\textcircled{1}$.

Figure 14 shows the comparison of cumulative AE energy under different vertical stress differences. When compared to the reference sample M15-0, the cumulative AE energy of M15-1 increases steadily; only the local stage increases slowly, indicating that the hydraulic fracture in the sample mainly propagates in the rock matrix. Although there is an opening phenomenon of the interface, it is not considerable. Figure 15 shows the statistical results of hydraulic fractures' area in the samples under different conditions of vertical stress. With the increase of vertical stress difference from 6 to 9 MPa , the total hydraulic fracture area decreases by 369.6 cm^2 ; the tensile fracture area increases by 96.2 cm^2 , and the shear fracture area decreases by 465.8 cm^2 . The normal stress on the interlayer interface is positively correlated with the vertical stress. Hence, the increase of the normal stress further increases the resistance of the interface to shear failure. Therefore, the increase of the vertical stress difference of the formation increases the hydraulic fractures' ability to penetrate the interfaces and interlayers, and the interaction patterns between the hydraulic fracture and interfaces gradually changes from II + III + IV to the

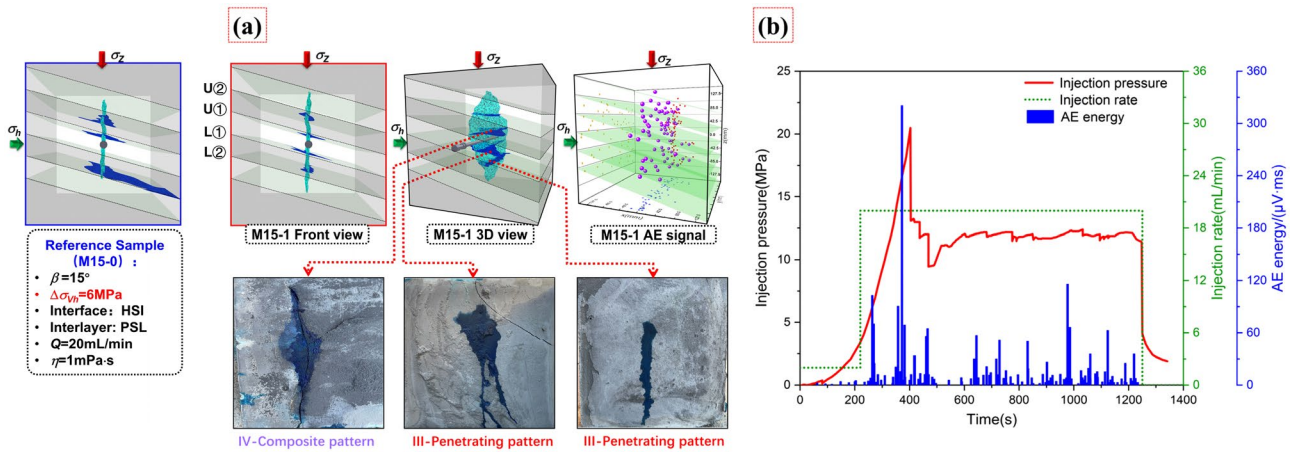


Fig. 13 HFE results of the sample when $\Delta\sigma_{vh}=9$ MPa (sample M15-1): **a** hydraulic fracture propagation pattern; **b** injection pressure curve and AE curve

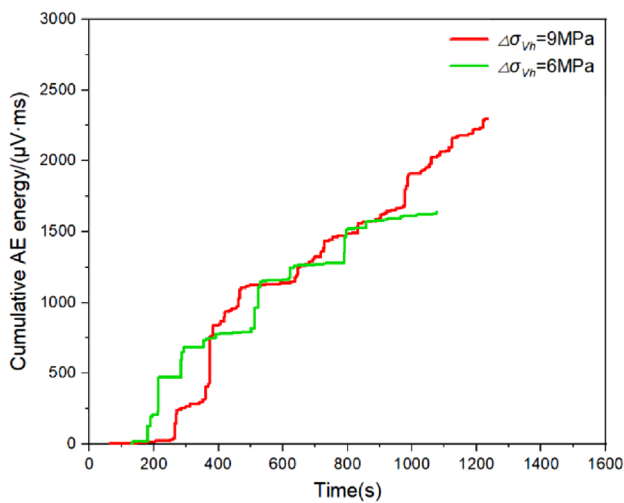


Fig. 14 Cumulative AE energy of samples with different vertical stress differences

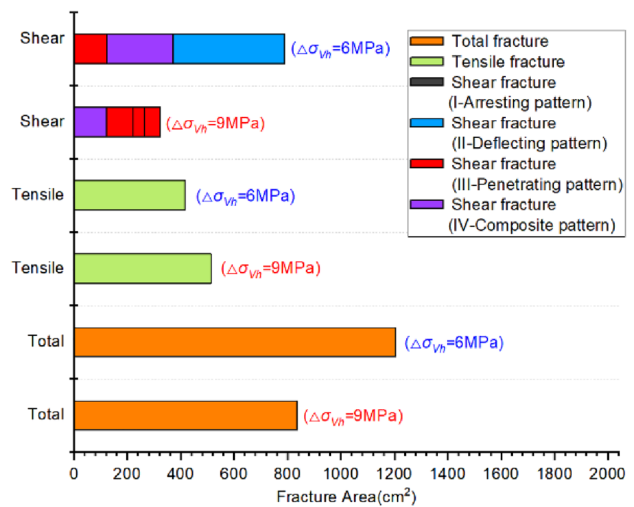


Fig. 15 Statistics of hydraulic fracture area of samples with different vertical stress differences

pattern dominated by III. The influence of the in situ stress difference offsets the deflection effect of the interlayer dip angle on the propagation direction of the artificial fracture to a certain extent. With the increase of the vertical in situ stress difference, the influence of the interface dip angle on the deflection of hydraulic fractures decreases, and the penetration ability of hydraulic fractures increases significantly.

Based on the mechanical parameters and experimental conditions of the samples, the Gu criterion (Gu et al. 2012) and the HFE results of this study are compared and analyzed, as shown in Fig. 16. The theoretical calculation results of Gu criterion show that the interaction patterns between the hydraulic fracture and weak interfaces are affected by the in situ stress difference and interface dip angle. The penetration ability of the hydraulic fractures is negatively

correlated to the interface dip angle, but positively correlated to the vertical stress difference. When the dip angle of the interface is too large, no matter how much the vertical in situ stress difference increases, it is challenging for the hydraulic fractures to penetrate the interface to communicate with the other pay layers. Most interaction patterns between the hydraulic fracture and interfaces in the four experimental groups herein are consistent with the theoretical calculation results. The partial deviation between the experimental results and the theoretical criterion is due to the nonuniformity of the interface.

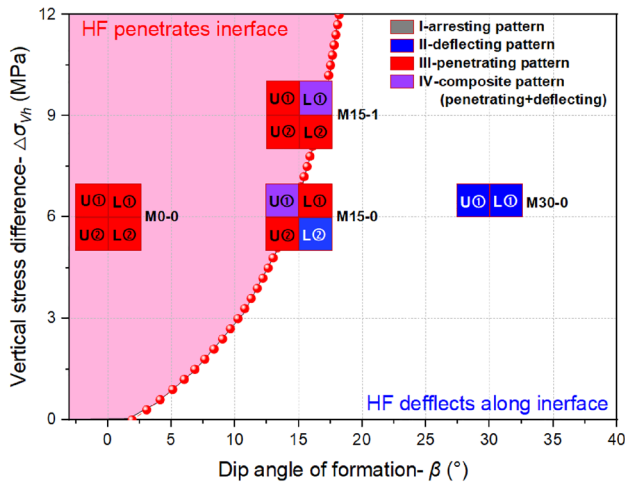


Fig. 16 Comparison between Gu criterion (Gu et al. 2012) and HFE results (the combined actions of the interlayer dip angle and vertical stress difference)

5.3 Influence of the Interface Cementation Strength

Figure 17 shows the HFE results of the sample within LSI (M15-2). In Fig. 17a, the upper end of the hydraulic fracture deflects along the interface U⊙, while the lower end of the fracture penetrates through the interface L⊙ into the sandstone interlayer, which is caused by not centering the injection pipe. It is challenging to ensure that the injection pipe is completely centered in the middle layer since the cement mortar shrinks after solidification. Additionally, in practical engineering, the horizontal well may not be completely in the middle of the pay zone, so this asymmetrical phenomenon is acceptable. After penetrating the interface L⊙, the lower end of the hydraulic fracture deflects and expands along the interface L⊙. With the increase of the interface

cementation strength, the possibility or degree of hydraulic fracture deflecting along the interface decreases and the fracture’s penetration ability and propagation in height improves. In Fig. 17b, the fracture initiation pressure of sample M15-2 is 17.89 MPa. At the initial stage of the hydraulic fracture propagation, the injection pressure curve shows a composite form of both large and small amplitude fluctuations, reflecting the *composite pattern* between the hydraulic fracture and interface L⊙. However, when $t = 635$ s, the pressure curve greatly decreases and maintains a small value in the subsequent stage, which is consistent with the *deflecting pattern* of the hydraulic fracture along interfaces U⊙ and L⊙.

Figure 18 shows the comparison of the cumulative AE energy of samples within HSIs and LSIs. The growth characteristics of the cumulative AE energy of M15-2 and the reference sample M15-0 are similar in the early stage, showing the characteristics of the *composite pattern*. However, the AE energy of M15-2 hardly increases in the later stage of fracturing, and the fracture propagation changes to the *deflecting pattern*. Figure 19 shows the statistical results of the hydraulic fracture area. When compared with M15-2 (within HSIs), the total hydraulic fracture area of M15-2 (within LSIs) increases by 506.9 cm²; the tensile fracture area decreases by 181.6 cm² and the shear fracture area increases by 688.5 cm². As the interface cementation strength changes from strong to weak, the interaction between the hydraulic fracture and interface gradually changes from II + III + IV pattern to the mode dominated by the *deflecting pattern*. Based on the above analysis, although the decrease of the interfacial cementation strength is beneficial for increasing the fracture propagation area, the disadvantages are at the cost of damaging the penetration ability of the hydraulic fractures. Therefore, hydraulic fractures in the interlayered shale oil reservoirs within relatively stable

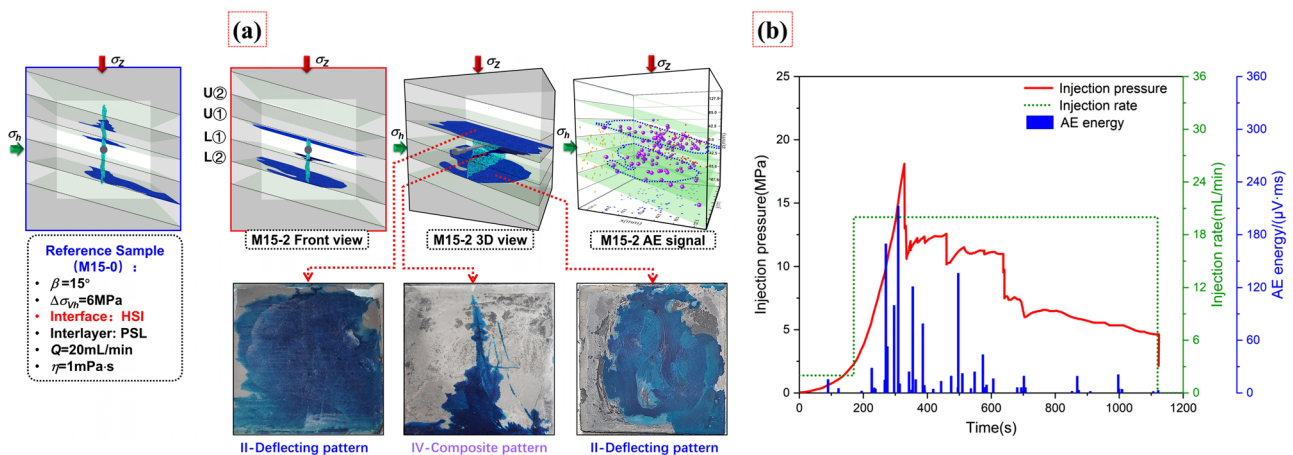


Fig. 17 HFE results of the sample within LSI (sample M15-2): **a** hydraulic fracture propagation patterns; **b** injection pressure and AE curves

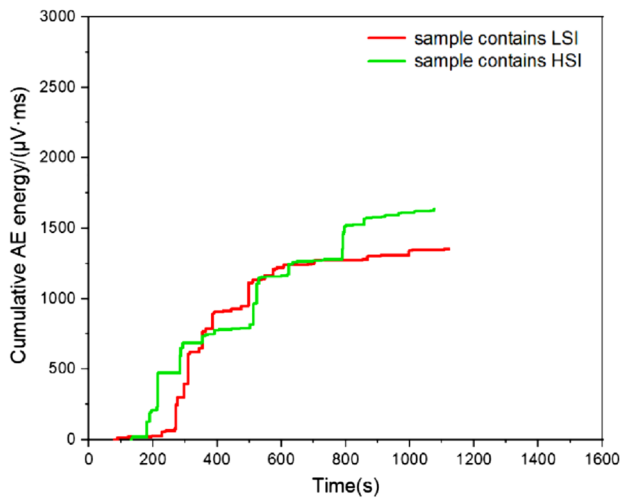


Fig. 18 Cumulative AE energy of samples within HSI and LSI

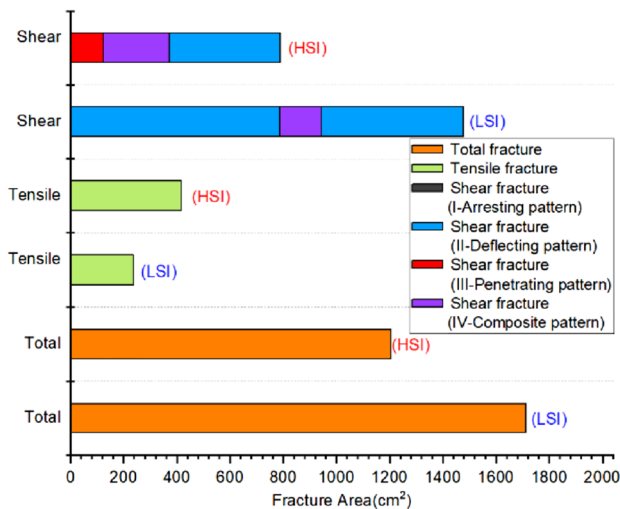


Fig. 19 Statistics of hydraulic fracture area of samples within HSI and LSI

interfaces can communicate more pay zones, achieving the purpose of the multilayer simultaneous recovery.

Figure 20 shows the comparison between the experimental results and Gu criterion under the combined action of the interface cementation strength and vertical stress difference. The results of the Gu criterion show that the penetration ability of hydraulic fractures is positively correlated with the interface cementation strength and vertical stress difference. According to the sample parameters and experimental conditions herein, when the vertical stress difference exceeds 15.05 MPa, the hydraulic fracture can penetrate the interface even when the interface does not

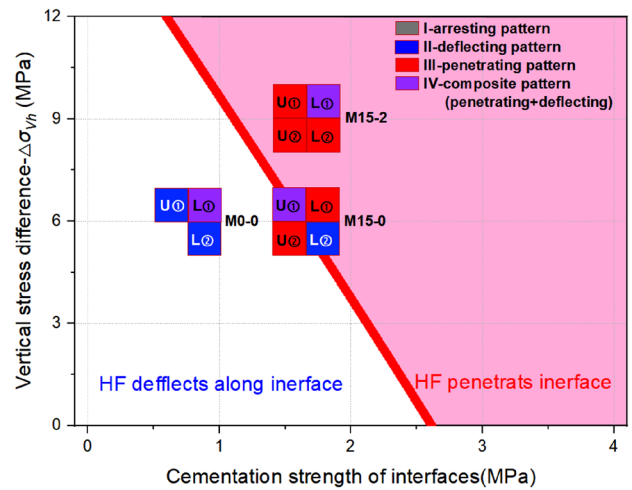


Fig. 20 Comparison of the Gu criterion (Gu et al. 2012) and HFE results (the combined action of interfacial cementation strength and vertical stress difference)

have cementation strength. At this time, the penetration ability of the hydraulic fracture is mainly controlled by interfacial friction resistance. Additionally, when the interface cementation strength exceeds 2.61 MPa, even if the vertical stress difference is 0, the hydraulic fracture can penetrate the interface and enter the interlayer. When considering the reference sample M15-0, its mechanical parameters and experimental conditions closely approach the critical curve calculated by the Gu criterion, yielding a composite propagation pattern; the results of the other samples are also consistent with the theoretical results.

5.4 Influence of the Interlayer Brittleness

Although rock brittleness is an important mechanical parameter to evaluate the hydraulic fracturing potential of shale oil reservoirs, few experiments have studied the relationship between rock brittleness and hydraulic fracture propagation behaviors because of the difficulty of obtaining large-scale rock outcrops with different brittleness. The advantage of the simulated materials selected herein is that they have significant brittleness and strength differences. Therefore, the true triaxial HFEs with samples containing different brittle interlayers are examined for the first time.

Figure 21 shows the HFE results of the sample within BSLs (M15-3). When compared to the reference sample M15-0 within PSLs, the hydraulic fracture in sample M15-3 has a stronger penetration ability and successively penetrates the upper and lower four interfaces. In Fig. 21a, the range of the filtered fracturing fluid on interface L⊙ is large, so the interaction between hydraulic fracture and L⊙ can be considered as the composite pattern. In Fig. 21b, the fracture initiation pressure of sample M15-3 is 19.00 MPa, which

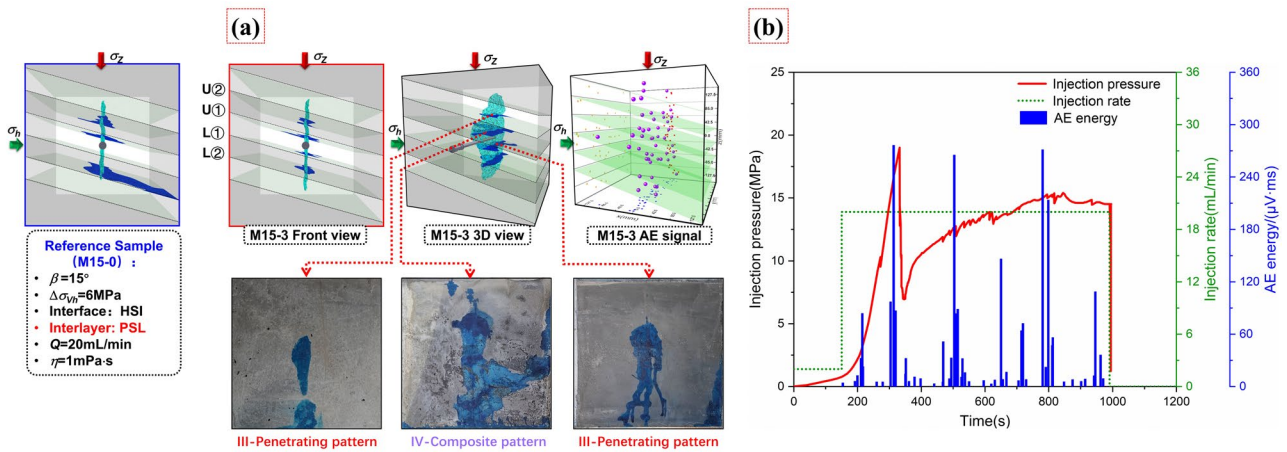


Fig. 21 HFE results of the sample within BSLs (sample M15-3): **a** hydraulic fracture propagation patterns; **b** injection pressure and AE curves

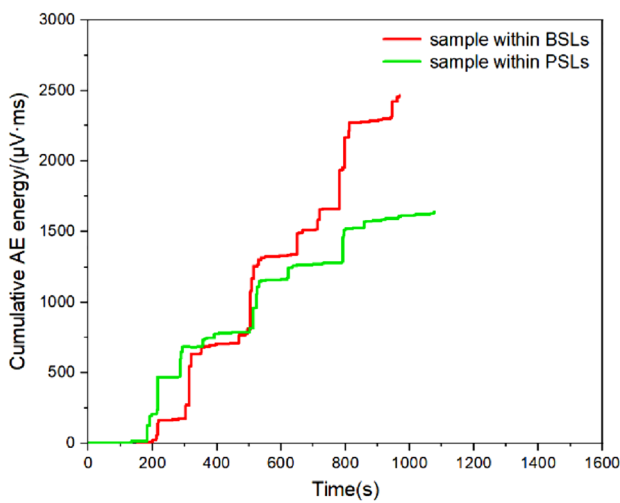


Fig. 22 Cumulative AE energy of samples within BSLs and PSLs

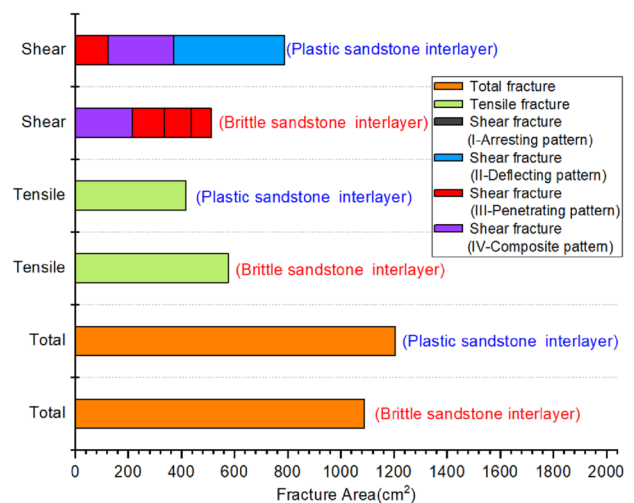


Fig. 23 Statistics of hydraulic fracture area of samples within BSLs and PSLs

is slightly lower than that of the reference sample M15-0, indicating that the increase of the interlayer brittleness may reduce the hydraulic fracture initiation pressure of the middle layer; however, the effect is not significant. The injection pressure curve suddenly decreases and subsequently increases after it reaches the initiation pressure. In the later propagation stage, the pressure curves are relatively stable, and only a small amplitude fluctuation occurs locally, which indicates that the hydraulic fractures mainly propagate in the shale layer and sandstone interlayer. In addition, when compared to the reference sample M15-0, there are a greater number of peaks of AE energy in the fracturing process of M15-3, which shows that the brittle fracture characteristics are more obvious when the hydraulic fracture propagates in the brittle interlayer.

Figure 22 shows the comparison of the cumulative AE energy of the samples within BSLs and PSLs. In the fracture initiation stage, the two AE energy curves rise stepwise, which corresponds to the brittle fracture characteristics of brittle shale between the two samples. However, during the fracture propagation stage, the increase of AE energy in BSLs in M15-2 is greater, and the brittle fracture characteristics are more obvious. Figure 23 shows the statistical results of the hydraulic fracture area of the samples. When compared to the reference sample M15-0, the total hydraulic fracture area of the sample M15-3 is reduced by 117.9 cm²; the tensile fracture area is increased by 159.6 cm², and the shear fracture area is reduced by 277.5 cm². The interaction between the hydraulic fracture and interfaces gradually changes from the II + III + IV composite pattern to the

III + IV composite pattern. Brittleness is the characteristic of rock failure with only small deformation under the action of external force, which reflects that the rock has obvious elastic deformation, but no obvious plastic deformation before failure (Ai et al. 2016). The low brittle interlayer has a certain plastic deformation that dissipates part of the elastic energy before the hydraulic fracture intersects with the interfaces; this effect reduces the hydraulic fracture penetration ability. Even when the hydraulic fracture penetrates the interface into the brittle interlayer, the plastic deformation of the interlayer further consumes the energy of the fracture propagation in the interlayer and inhibits the hydraulic fracture propagation. Conversely, when the fracture propagates in the high brittle interlayer, the rock is characterized mainly by elastic deformation, and the energy dissipation caused by plastic deformation is relatively small. The release of the high elastic properties produces multiple branch fractures, especially in the high brittle interlayer (Zhang et al. 2018). Therefore, shale brittleness should not only be used as the evaluation standard of the hydraulic fracturing ability and potential of the sandstone–shale interlayered formation; the plastic–brittleness characteristics of the sandstone interlayers should also be considered. When considering the appropriate method for the formation with strong plastic sandstone interlayer, separate layered hydraulic fracturing is more suitable.

6 Influence of the Fracturing Treatment Parameters on Fracture Propagation Behavior in the Sandstone–Shale Interlayered Formation

In the actual fracturing engineering, not all interlayered shale oil reservoirs have ideal reservoir properties. In this section, the HFEs are conducted to further clarify the effects

of two key controllable parameters, namely, fluid injection rate and fracturing fluid viscosity, on the hydraulic fracture penetration and propagation.

6.1 Influence of the Fluid Injection Rate

Figure 24a shows the HFE results of the sample under $Q = 10$ mL/min. The lower end of the hydraulic fracture deflects along the interface L①, while the upper end of the hydraulic fracture penetrates U① and shows the propagation with the *composite pattern*. Subsequently, the hydraulic fracture deflects and expands along U②; however, the range of the fracturing fluid leakage into the interface is small. In Fig. 24b, the fracture initiation pressure of sample M15-4 is 14.58 MPa, which is less than that of the reference sample M15-0, indicating a positive correlation between the fracture initiation pressure and fluid injection rate. The injection pressure curve of sample M15-4 is relatively stable with a small fluctuation during the fracture propagation stage, which corresponds to the *penetrating pattern* when the hydraulic fracture encounters the interfaces. However, the injection pressure curve decreases greatly at 872 s, which reflects that the hydraulic fracture deflects and expands along the interface L①. The AE signals and energy are considerable during the fracture initiation stage and the early fracture propagation stage, whereas their AE signal frequency and energy values are significantly reduced when the hydraulic fracture deflects and expands along the interface.

Figure 25 shows the comparison of the cumulative AE energy of the samples under different injection rates. When the fluid injection rate is high (20 mL/min), the distribution of AE events in sample M15-0 is concentrated near the pressure fluctuation point. Although the number of the fracture events is small, the AE energy value is high, indicating high-speed dynamic propagation of the

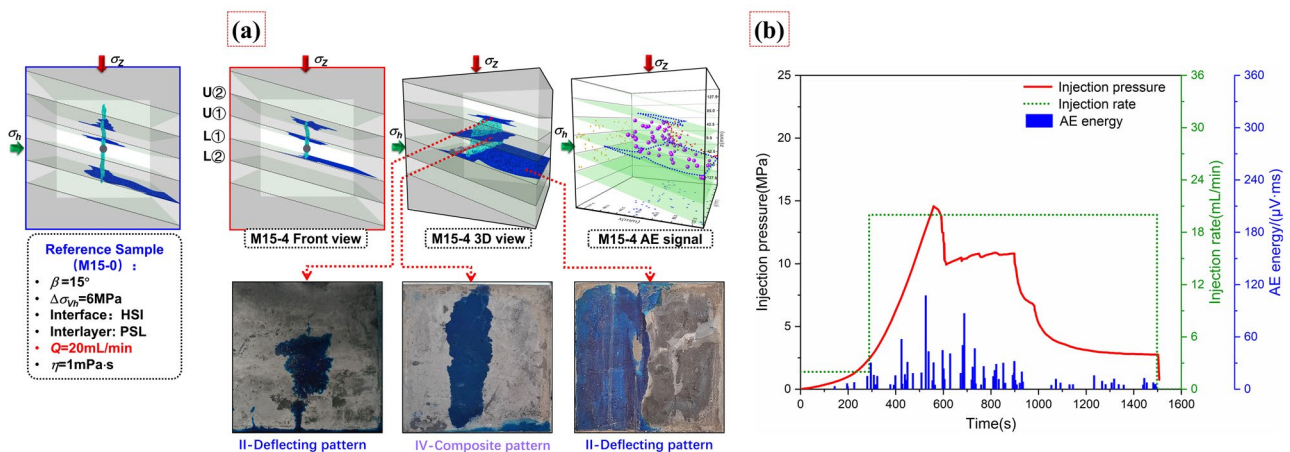


Fig. 24 HFE results of the sample when $Q = 10$ mL/min (sample M15-4): **a** hydraulic fracture propagation patterns; **b** injection pressure and AE curves

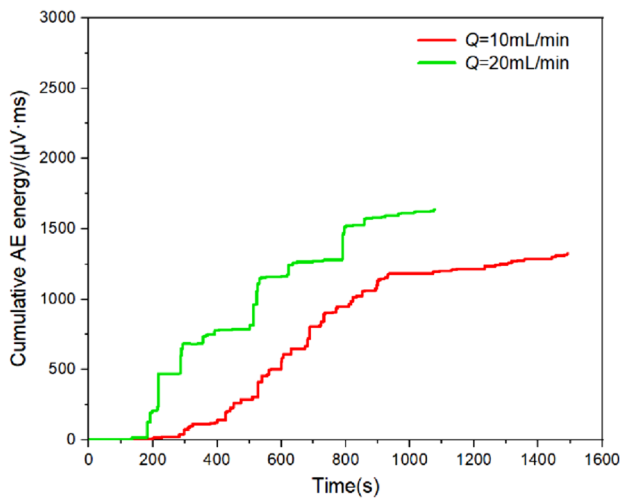


Fig. 25 Cumulative AE energy of samples under different fluid injection rates

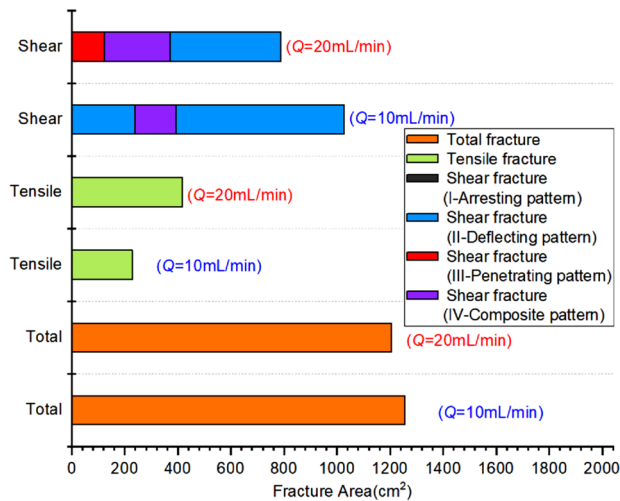


Fig. 26 Statistics of hydraulic fracture area of samples under different fluid injection rates

hydraulic fractures. Conversely, under the low fluid injection rate (10 mL/min), there are more AE events with relatively uniform distribution and a slower growth rate of total cumulative AE energy, indicating that the fractures in sample M15-4 have the characteristic of low-speed steady-state propagation. In addition, when the hydraulic fracture in M15-4 deflects and expands along the interface, the AE energy hardly increases. Figure 26 shows the statistical results of the hydraulic fracture area of the samples under different fluid injection rates. When compared to sample M15-0, the total hydraulic fracture area of M15-4 increases by 50.3 cm²; the tensile fracture area decreases by 188.3 cm², and the shear fracture area increases by

238.6 cm². The decrease in the fluid injection rate makes the interaction between the hydraulic fracture and the interfaces gradually change from the II + III + IV pattern to the pattern dominated by deflection. When a low fluid injection rate is used for hydraulic fracturing treatment in the interlayered shale oil formation, the fracturing fluid easily filters, flows, and distributes hydraulic energy along the microfractures at the intersection, leading to a decrease in the net pressure and penetration ability of the hydraulic fracture and forcing it to stop at the interface or to deflect along the open interface. With an increase in the fracturing fluid injection rate, the hydraulic energy of the fracture is more concentrated, which reduces the filtration along the interface and is conducive to the hydraulic fractures' penetration into more pay zones.

6.2 Influence of the Fracturing Fluid Viscosity

Figure 27a shows the HFE results under high-pressure fracturing fluid viscosity ($\eta = 25$ mPa s). In sample M15-5, the upper end of the hydraulic fracture successively penetrates the interfaces U[⊙] and U[⊙], while the lower end of the hydraulic fracture penetrates the interface L[⊙] and has a *composite pattern* interaction with the interface L[⊙]. This is because there is a large range of fracturing fluid filtration on the interface L[⊙]. The viscosity of the fracturing fluid mainly controls the fracture propagation behavior by controlling the fluid filtration. The high-viscosity fracturing fluid has the characteristics of small filtration in the interfaces, thus increasing the propagation ability of the hydraulic fractures in the rock matrix. In Fig. 27b, the fracture initiation pressure of sample M15-5 is 23.89 MPa, which is higher than that of the reference sample M15-0, showing that there is a positive correlation between the fracture initiation pressure and fracturing fluid viscosity. The injection pressure curve of sample M15-5 has no violent fluctuation during the entire propagation stage. Furthermore, the distribution of AE events is relatively scattered with many high-energy points, indicating that the stable propagation of hydraulic fracture is accompanied by significant rock fracture driven by high-viscosity fluid.

Figure 28 shows the comparison of cumulative AE energy of samples under different fracturing fluid viscosities. The cumulative AE energy curve under the low fluid viscosity increases slowly and finally stabilizes in the later stage of fracture propagation, reflecting the deflection along the interface. Meanwhile, the curve under the high fluid viscosity maintains a stable increase in the entire stage, corresponding to the penetration of the hydraulic fracture through the interface into the interlayered rock matrix. Figure 29 shows the statistical results of the hydraulic fracture area of the samples under different fracturing fluid viscosities. When compared to sample M15-0, the total hydraulic fracture area of M15-5

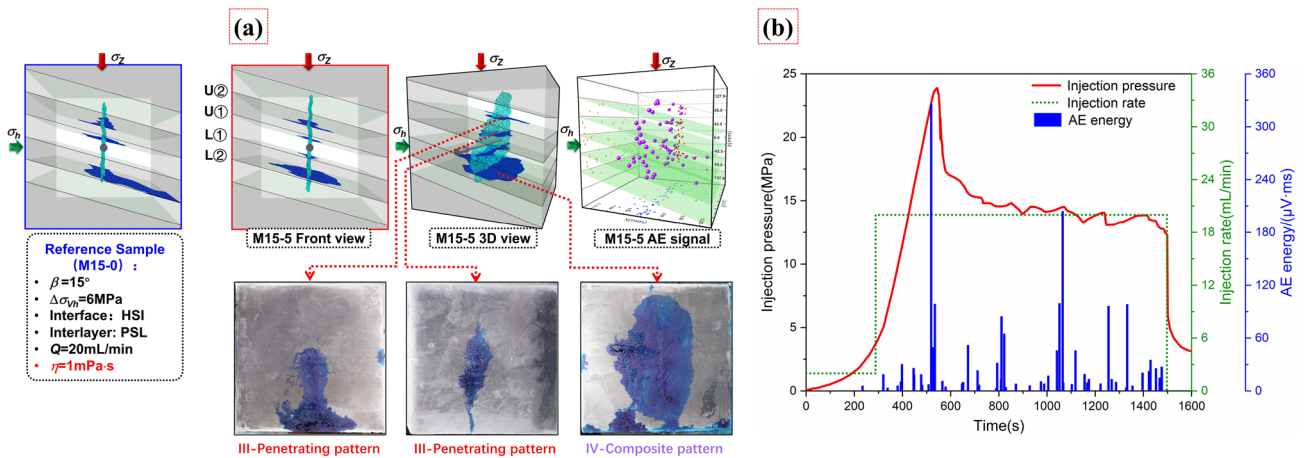


Fig. 27 HFE results of the sample when $\eta=25 \text{ mPa s}$ (sample M15-5): **a** hydraulic fracture propagation patterns; **b** injection pressure and AE curves

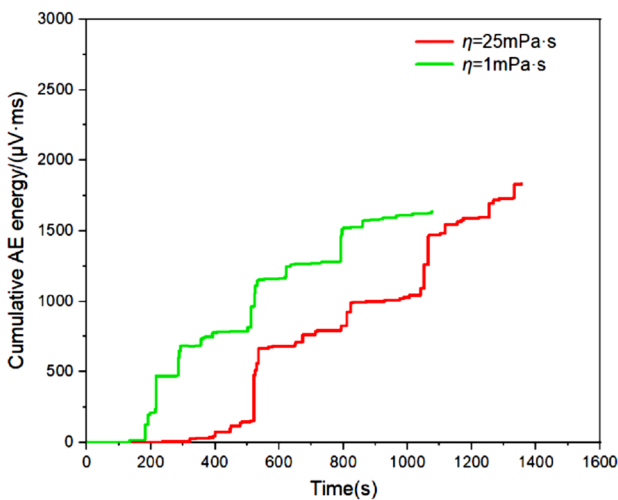


Fig. 28 Cumulative AE energy of samples under different fracturing fluid viscosities

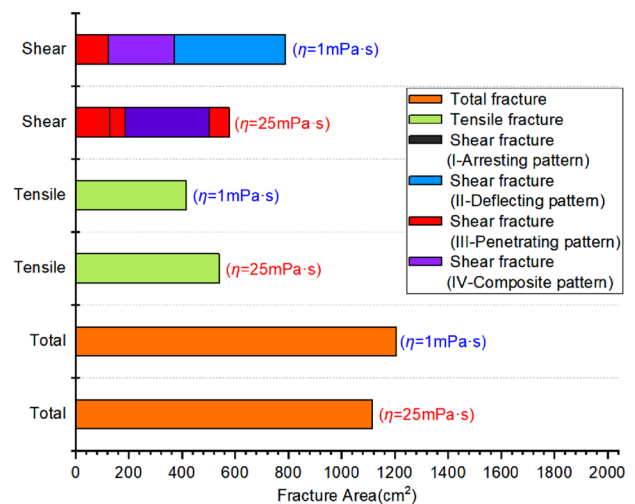


Fig. 29 Statistics of hydraulic fracture area of samples under different fracturing fluid viscosities

decreases by 88.55 cm^2 ; the shear fracture area increases by 211.66 cm^2 , but the tensile fracture area increases by 123.05 cm^2 . Moreover, with the increase of the fracturing fluid viscosity, the interaction between the hydraulic fracture and interfaces gradually changes from type II + III + IV patterns to the *penetrating pattern*. The low-viscosity fracturing fluid promotes the infiltration of the fracturing fluid along the interfaces and induces the shear slip, dilation, and opening of the interfaces, which is beneficial to increase the fracture propagation area. However, the low-viscosity fracturing fluid reduces the hydraulic energy to maintain the fracture propagating in the rock matrix, thereby reducing the penetration ability of the fracture. Properly increasing the viscosity of the fluid maintains a high net pressure in the fracture and

ensures the penetration propagation through the upper and lower sandstone interlayers to obtain a more effective fracture height. However, very high viscosity of the fracturing fluid produces negative problems, which reduce the ability of the hydraulic fractures to communicate with natural fractures and increase the complexity of fracture network in the fracture length direction. Therefore, fracturing fluids with different viscosities at different stages of the fracturing operation should be used. Thus, the penetration ability of the hydraulic fractures near the wellbore can be increased through the high-viscosity fracturing fluid. When multiple pay zones along the fracture's height have been communicated, the low-viscosity fracturing fluid can be further used to increase the ability of

the fractures to communicate with natural fractures along the fracture's length.

7 Discussion and Conclusion

First, the conclusions of this study can play a qualitative guiding role to improve the hydraulic fracturing design of the sandstone–shale formation. However, the practical application of the test scale results to the hydraulic fracturing operation of a field-scale reservoir requires further research. Although HFE is the most intuitive approach to explore fracture propagation behaviors, laboratory fracturing equipment cannot fully simulate the real-world hydraulic fracturing conditions, especially because the sample size, borehole size, and pumping rate in a laboratory experiment are far smaller than those on the field scale (Zhao et al. 2019; Chen et al. 2020a). Currently, few studies address the large-scale effects of HFE. Establishing a similar criterion of the sandstone–shale interlayered formation to quantitatively enlarge the HFE results to the field size is a crucial point for future research. In addition, the two most important controllable treatment parameters on field are the injection rate and fracturing fluid viscosity; these parameters greatly affect the propagation of fractures in the sandstone–shale interlayered formation. However, the injection rate and fluid viscosity are positively correlated to the hydraulic fracture penetration ability along the height of the fractures but negatively correlated with the ability of the hydraulic fracture to communicate with the natural fractures along the length of the fractures. Therefore, it is challenging to maintain the fracture height and complexity along the fracture length simultaneously by adjusting these two fracturing construction parameters alone. This contradiction can be ameliorated by alternately injecting fluids with different rates and viscosities (Zhou et al. 2017; Xin 2019; Sun et al. 2020). However, the timing and amplitude of the change in the injection rate and the injection stage of fracturing fluids with different viscosities must be studied in combination with the reservoir condition, which will be further examined using the experimental model. Finally, this study focuses on the propagation mechanism of single fractures in a sandstone–shale interlayered formation. However, the multiple-cluster hydraulic fracturing technology has been applied for interlayered shale oil formations in many well areas. Hence, there is a competitive effect between initiation and propagation among multiple fractures (Liu et al. 2019a, b; Chen et al. 2020b). Whether the competitive effect among the multiple fractures in terms of propagation affects the fracture propagation and penetration through the interlayers must be studied further using experimental models combined with numerical simulations and theoretical analysis.

To investigate the vertical propagation mechanism of hydraulic fractures in the sandstone–shale interlayered

formation, a simulated interlayered experimental model was designed herein based on the relative mechanical characteristics of the sandstone and shale layers in the Qingyi member. Through a series of HFEs, the influence of different key factors on the hydraulic fracture propagation behavior was analyzed, and the following conclusions were obtained.

- (1) There may be three types of microcracks in FPZ at the hydraulic fracture tip before it intersects with the interlayer interface. Under the influence of different combined forms of microcracks, the possible propagation of hydraulic fractures in the sandstone–shale interlayered formation includes the following: I—*arresting pattern*, II—*deflecting pattern*, III—*penetrating pattern*, and IV—*multicomposite pattern*.
- (2) With the increasing interlayer dip angle, the hydraulic fracture propagation gradually changes from the *penetrating pattern* to the *deflecting pattern*, which increases the shear fracture area obtained by the deflection and extension of the hydraulic fracture along the interfaces, but inhibits the penetration ability of the hydraulic fracture. To communicate multiple shale formations through one hydraulic fracturing operation, it is critical to select the formation with a small dip angle.
- (3) The penetration ability of the hydraulic fracture has a positive correlation with the vertical in situ stress difference and the interface cementation strength. When the dip angle of the interface is too large (approximately 25° herein), it is challenging for hydraulic fractures to penetrate the interface, irrespective of the increase in the vertical in situ stress difference. When the vertical in situ stress difference is sufficiently large (15.05 MPa herein), the hydraulic fracture can penetrate through the interface into the interlayer even when the interface cementation strength is 0.
- (4) When compared within the PSLs, the tensile fracture area caused by the fracture propagation in BSLs increases. Under the same conditions, it is easier for hydraulic fractures to penetrate the interface into the BSLs. The plastic deformation of the low brittle interlayer dissipates part of the elastic energy used to maintain the hydraulic fracture propagation and inhibits the ability of the hydraulic fractures to penetrate the interlayer.
- (5) Properly increasing the fluid viscosity promotes the hydraulic fracture to penetrate the upper and lower sandstone interlayers, obtaining a larger fracture height. However, to maintain the propagation range of the hydraulic fractures' length when multiple shale layers along the fractures' height have been communicated, low-viscosity fracturing fluid should be used to increase

the ability of the fractures to communicate natural fractures along the fractures' length.

Author Contributions JZ: methodology, writing—original draft, investigation. QY: writing—original draft, investigation. YL: methodology, investigation, writing—review and editing. ZP: writing—review and editing, validation. BL: data curation.

Funding The research was supported by the project of “National Natural Science Foundation of China (52004065, 52174024)”, “Nature Scientific Foundation of Heilongjiang Province (YQ2021E006)” and “Research start project of Northeast Petroleum University (No. 1305021857)”.

Data Availability The data used to support the findings of this study are available from the corresponding author upon request.

Declarations

Conflict of interest The authors declare that they have no known competing financial interests or personal relationships that could have influenced the work reported in this paper.

References

- Ai C, Zhang J, Li YW, Zeng J, Yang XL, Wang JG (2016) Estimation criteria for rock brittleness based on energy analysis during the rupturing process. *Rock Mech Rock Eng* 49(12):4681–4698. <https://doi.org/10.1007/s00603-016-1078-x>
- Aimene Y, Hammerquist C, Ouenes A (2019) Anisotropic damage mechanics for asymmetric hydraulic fracture height propagation in a layered unconventional gas reservoir. *J Nat Gas Sci Eng* 67:1–13. <https://doi.org/10.1016/j.jngse.2019.04.013>
- Athavale AS, Miskimins JL (2008) Laboratory hydraulic fracturing tests on small homogeneous and laminated blocks. ARMA-08-067
- Blanton TL (1986) Propagation of hydraulically and dynamically induced fractures in naturally fractured reservoirs. *SPE* 15261-MS. <https://doi.org/10.2118/15261-MS>
- Cao SR, Li XY, Zhou Z, Wang YW, Ding H (2020) Investigation of hydraulic fracturing crack propagation behavior in multi-layered coal seams. *Appl Sci* 10(3):1153. <https://doi.org/10.3390/app10031153>
- Casas LA, Miskimins JL, Black AD, Green SJ (2006) Hydraulic fracturing laboratory test on a rock with artificial discontinuities. *SPE* 103617-MS. <https://doi.org/10.2118/103617-MS>
- Chen M, Zhang SC, Xu Y, Ma XF, Zou YS (2020a) A numerical method for simulating planar 3D multi-fracture propagation in multi-stage fracturing of horizontal wells. *Pet Explor Dev* 47(1):171–183. [https://doi.org/10.1016/S1876-3804\(20\)60016-7](https://doi.org/10.1016/S1876-3804(20)60016-7)
- Chen Z, Li XB, Cao H, Huang LQ (2020b) Experimental investigation of the influence of pulsating hydraulic fracturing on pre-existing fractures propagation in coal. *J Pet Sci Eng* 189:107040. <https://doi.org/10.1016/j.petrol.2020.107040>
- Cheng P, Zhang CP, Ma ZY, Zhou JP, Zhang D, Liu XF, Ranjith PG (2022) Experimental study of micromechanical properties alterations of shale matrix treated by ScCO₂-Water saturation using nanoindentation tests. *Energy* 242:122965. <https://doi.org/10.1016/j.energy.2021.122965>
- Chong ZH, Yao QL, Li XH (2019) Experimental investigation of fracture propagation behavior induced by hydraulic fracturing in anisotropic shale cores. *Energies* 12(6):976. <https://doi.org/10.3390/en12060976>
- Cong ZY, Li YW, Pan YS, Liu B, Shi Y, Wei JG, Li W (2022a) Study on CO₂ foam fracturing model and fracture propagation simulation. *Energy* 238:121778. <https://doi.org/10.1016/j.energy.2021.121778>
- Cong Z, Li Y, Tang J, Dmitriy A, Hubuqin YF (2022b) Numerical simulation of hydraulic fracture height layer-through propagation based on three-dimensional lattice method. *Eng Fract Mech* 264:108331. <https://doi.org/10.1016/j.engfracmech.2022.108331>
- Daneshy AA (1978) Hydraulic fracture propagation in layered formations. *SPE J* 18(1):33–41. <https://doi.org/10.2118/6088-PA>
- El W (1987) Hydraulic fracture propagation in the presence of stress variation. *SPE* 16898-MS. <https://doi.org/10.2523/16898-MS>
- Fraser-Harris AP, Mcdermott CI, Couples GD, Edlmann K, Lightbody A, Cartwright-Taylor A, Kendrick JE, Brondolo F, Fazio M, Sauter M (2020) Experimental investigation of hydraulic fracturing and stress sensitivity of fracture permeability under changing polyaxial stress conditions. *J Geophys Res-Sol Earth* 125(12):e2020JB020044. <https://doi.org/10.1029/2020JB020044>
- Fu W, Ames BC, Bunger AP, Savitski AA (2016) Impact of partially cemented and non-persistent natural fractures on hydraulic fracture propagation. *Rock Mech Rock Eng* 49:4519–4526. <https://doi.org/10.1007/s00603-016-1103-0>
- Gao Q, Cheng YF, Yan CL (2018) A 3D numerical model for investigation of hydraulic fracture configuration in multilayered tight sandstone gas reservoirs. *J Pet Explor Prod Technol* 8:1413–1424. <https://doi.org/10.1007/s13202-017-0417-0>
- Gu H, Weng X, Lund JB, Mack MG, Ganguly U, Suarez-Rivera R (2012) Hydraulic fracture crossing natural fracture at non-orthogonal angles, a criterion, its validation and applications. *SPE* 139984-MS. <https://doi.org/10.2118/139984-MS>
- Guo TK, Zhang SC, Qu ZQ, Zhou T, Xiao YS, Gao J (2014) Experimental study of hydraulic fracturing for shale by stimulated reservoir volume. *Fuel* 128:373–380. <https://doi.org/10.1016/j.fuel.2014.03.029>
- Guo JC, Luo B, Zhu HY, Yuan SH, Deng Y, Duan YJ, Duan WG (2016) Multilayer stress field interference in sandstone and mudstone thin interbed reservoir. *J Geophys Eng* 13(5):775–785. <https://doi.org/10.1088/1742-2132/13/5/775>
- Huang BX, Liu JW (2017) Experimental investigation of the effect of bedding planes on hydraulic fracturing under true triaxial stress. *Rock Mech Rock Eng* 50:2627–2643. <https://doi.org/10.1007/s00603-017-1261-8>
- Inskip NF, Browning J, Meredith PG, Gudmundsson A (2020) Conditions for fracture arrest in layered rock sequences. *Result Geophys Sci* 1–4:100001. <https://doi.org/10.1016/j.ringps.2020.100001>
- Ju Y, Wang YL, Xu B, Chen JL, Yang YM (2019) Numerical analysis of the effects of bedded interfaces on hydraulic fracture propagation in tight multilayered reservoirs considering hydro-mechanical coupling. *J Pet Sci Eng* 178:356–375. <https://doi.org/10.1016/j.petrol.2019.03.049>
- Li DQ, Zhang SC, Zhang SA (2014) Experimental and numerical simulation study on fracturing through interlayer to coal seam. *J Nat Gas Sci Eng* 21:386–396. <https://doi.org/10.1016/j.jngse.2014.08.022>
- Li YW, Jia D, Rui ZH, Peng JY, Fu CK, Zhang J (2017) Evaluation method of rock brittleness based on statistical constitutive relations for rock damage. *J Pet Sci Eng* 153:123–132. <https://doi.org/10.1016/j.petrol.2017.03.041>
- Li YW, Long M, Zuo LH, Li W, Zhao WC (2019) Brittleness evaluation of coal based on statistical damage and energy evolution

- theory. *J Pet Sci Eng* 172:753–763. <https://doi.org/10.1016/j.petrol.2018.08.069>
- Li TJ, Tang CA, Rutqvist J, Hu MS, Li LC, Zhang LY, Huang B (2020a) The influence of an interlayer on dual hydraulic fractures propagation. *Energies* 13(3):555. <https://doi.org/10.3390/en13030555>
- Li YW, Long M, Tang JZ, Chen M, Fu XF (2020b) A hydraulic fracture height mathematical model considering the influence of plastic region at fracture tip. *Pet Explor Dev* 47:184–195. [https://doi.org/10.1016/S1876-3804\(20\)60017-9](https://doi.org/10.1016/S1876-3804(20)60017-9)
- Li MH, Zhou FJ, Yuan LS, Chen L, Hua XD, Huang GP, Han SB (2021) Numerical modeling of multiple fractures competition propagation in the heterogeneous layered formation. *Energy Rep* 7:3737–3749. <https://doi.org/10.1016/j.egy.2021.06.061>
- Liu CL, Wang ZL, Guo ZQ, Hong WY, Dun C, Zhang X, Li B, Wu LQ (2017) Enrichment and distribution of shale oil in the Cretaceous Qingshankou Formation, Songliao Basin, Northeast China. *Mar Pet Geol* 86:751–770. <https://doi.org/10.1016/j.marpetgeo.2017.06.034>
- Liu B, Jin L, Hu C (2019a) Fractal characterization of silty beds/laminae and its implications for the prediction of shale oil reservoirs in Qingshankou Formation of Northern Songliao Basin, Northeast China. *Fractals* 27(1):1940009. <https://doi.org/10.1142/S0218348X19400097>
- Liu XQ, Qu ZQ, Guo TK, Sun Y, Wang ZY, Bakhshib E (2019b) Numerical simulation of non-planar fracture propagation in multi-cluster fracturing with natural fractures based on lattice methods. *Eng Fract Mech* 220:106625. <https://doi.org/10.1016/j.engfracmech.2019.106625>
- Llanos EM, Jeffrey RG, Hillis R, Zhang X (2017) Hydraulic fracture propagation through an orthogonal discontinuity: a laboratory, analytical and numerical study. *Rock Mech Rock Eng* 50:2101–2118. <https://doi.org/10.1007/s00603-017-1213-3>
- Lu C, Lu XY, Guo JC, Liu LM (2020) Stability of the formation interface under the impact of hydraulic fracture propagation in the vicinity of the formation interface. *Pet Sci* 17:1101–1118. <https://doi.org/10.1007/s12182-019-00416-x>
- Luo L, Tan DP, Zha XJ, Tan XF, Gao XB (2021) Enrichment factors and resource potential evaluation of Qingshankou formation lacustrine shale oil in the Southern Songliao Basin, NE China. *Geofluids* 1:1–20. <https://doi.org/10.1155/2021/6645467>
- Renshaw CE, Pollard DD (1995) An experimentally verified criterion for propagation across unbounded interfaces in brittle linear elastic materials. *Int J Rock Mech Min* 32(3):237–249. [https://doi.org/10.1016/0148-9062\(94\)00037-4](https://doi.org/10.1016/0148-9062(94)00037-4)
- Roundtree R, Miskimins JL (2016) Experimental validation of micro seismic emissions from a controlled hydraulic fracture in a synthetic layered medium. *SPE* 140653-MS. <https://doi.org/10.2118/140653-MS>
- Sarmadivaleh M, Rasouli V (2015) Test design and sample preparation procedure for experimental investigation of hydraulic fracturing interaction modes. *Rock Mech Rock Eng* 48(1):93–105. <https://doi.org/10.1007/s00603-013-0543-z>
- Song Z, Zhang Z, Zhang G, Huang J, Wu M (2022) Identifying the types of loading mode for rock fracture via convolutional neural networks. *J Geophys Res-Sol Earth* 127(2):e2021JB022532. <https://doi.org/10.1029/2021JB022532>
- Sun C, Zheng H, Liu WD, Lu W (2020) Numerical investigation of complex fracture network creation by cyclic pumping. *Eng Fract Mech* 233:107103. <https://doi.org/10.1016/j.engfracmech.2020.107103>
- Tan P, Jin Y, Han K, Hou B, Chen M, Guo XF, Gao J (2017) Analysis of hydraulic fracture initiation and vertical propagation behavior in laminated shale formation. *Fuel* 206:482–493. <https://doi.org/10.1016/j.fuel.2017.05.033>
- Tan P, Jin Y, Xiong ZY, Mian C, Hou B (2018) Effect of interface property on hydraulic fracture vertical propagation behavior in layered formation based on discrete element modeling. *J Geophys Eng* 15(4):1542–1550. <https://doi.org/10.1088/1742-2140/aaa8ab>
- Tan P, Jin Y, Yuan L, Xiong ZY, Hou B, Chen M, Wan LM (2019) Understanding hydraulic fracture propagation behavior in tight sandstone–coal interbedded formations: an experimental investigation. *Pet Sci* 16:148–160. <https://doi.org/10.1007/s12182-018-0297-z>
- Tan P, Jin Y, Pang HW (2021) Hydraulic fracture vertical propagation behavior in transversely isotropic layered shale formation with transition zone using XFEM-based CZM method. *Eng Fract Mech* 248:107707. <https://doi.org/10.1016/j.engfracmech.2021.107707>
- Tang J, Wu K, Zuo L, Xiao L, Sun S, Ehlig-Economides C (2019) Investigation of rupture and slip mechanisms of hydraulic fracture in multiple-layered formation. *SPE J* 24(05):2292–2307. <https://doi.org/10.2118/197054-PA>
- Tang J, Fan B, Xiao L, Tian S, Zhang F, Zhang L, Weitz D (2021) A new ensemble machine learning framework for searching sweet spots in shale reservoirs. *SPE J* 26(01):482–497. <https://doi.org/10.2118/204224-PA>
- Wan L, Chen M, Hou B, Kao J, Zhang K, Fu W (2018) Experimental investigation of the effect of natural fracture size on hydraulic fracture propagation in 3D. *J Struct Geol* 116:1–11. <https://doi.org/10.1016/j.jsg.2018.08.006>
- Wang Y, Li X, He JM, Zhao ZH, Zheng B (2016) Investigation of fracturing network propagation in random naturally fractured and laminated block experiments. *Energies* 9(8):588. <https://doi.org/10.3390/en9080588>
- Wang Y, Hou B, Wang D, Jia Z (2021) Features of fracture height propagation in cross-layer fracturing of shale oil reservoirs. *Pet Explor Dev* 48(2):469–479. [https://doi.org/10.1016/S1876-3804\(21\)60038-1](https://doi.org/10.1016/S1876-3804(21)60038-1)
- Wu S, Li TT, Ge HK, Wang XQ, Li N, Zou YS (2019) Shear-tensile fractures in hydraulic fracturing network of layered shale. *J Pet Sci Eng* 183:106428. <https://doi.org/10.1016/j.petrol.2019.106428>
- Xie J, Tang J, Yong R, Fan Y, Li YW (2020) A 3-D hydraulic fracture propagation model applied for shale gas reservoirs with multiple bedding planes. *Eng Fract Mech* 228:106872. <https://doi.org/10.1016/j.engfracmech.2020.106872>
- Xin C (2019) Laboratory analysis of liquid injection method on hydraulic fracturing initiation and propagation in deep shale formation. *Nat Gas Ind B* 6:652–658. <https://doi.org/10.1016/j.ngib.2019.11.001>
- Xu D, Hu RL, Gao W, Xia JG (2015) Effects of laminated structure on hydraulic fracture propagation in shale. *Pet Explor Dev* 42(4):573–579. [https://doi.org/10.1016/S1876-3804\(15\)30052-5](https://doi.org/10.1016/S1876-3804(15)30052-5)
- Xue Y, Liu J, Ranjith PG, Gao F, Xie H, Wang J (2022) Changes in microstructure and mechanical properties of low-permeability coal induced by pulsating nitrogen fatigue fracturing tests. *Rock Mech Rock Eng*. <https://doi.org/10.1007/s00603-022-03031-2>
- Zhang F, Dontsov E, Mack M (2017) Fully coupled simulation of hydraulic fracture interacting with natural fractures with a hybrid discrete-continuum method. *Int J Numer Anal Methods* 41(13):1430–1452. <https://doi.org/10.1002/nag.2682>
- Zhang J, Ai C, Li YW, Che GM, Gao R, Zeng J (2018) Energy-based brittleness index and acoustic emission characteristics of anisotropic coal under triaxial stress condition. *Rock Mech Rock Eng* 51:3343–3360. <https://doi.org/10.1007/s00603-018-1535-9>
- Zhang F, Damjanac B, Maxwell S (2019) Investigating hydraulic fracturing complexity in naturally fractured rock masses using fully coupled multiscale numerical modeling. *Rock Mech Rock Eng* 52(12):5137–5160. <https://doi.org/10.1007/s00603-019-01851-3>
- Zhang JF, Xu XY, Bai J, Liu WB, Chen S, Liu C, Li YH (2020a) Enrichment and exploration of deep lacustrine shale oil in the

- first member of Cretaceous Qingshankou Formation, Southern Songliao Basin, NE China. *Petrol Explor Dev* 47(4):683–698. [https://doi.org/10.1016/S1876-3804\(20\)60085-4](https://doi.org/10.1016/S1876-3804(20)60085-4)
- Zhang J, Li YW, Li W, Chen ZJ, Zhao Y, Yu FH, Zheng Y (2020b) Study on propagation behaviors of hydraulic fracture network in tight sandstone formation with closed cemented natural fractures. *Geofluids*. <https://doi.org/10.1155/2020/8833324>
- Zhang X, Zhang YQ, Huang BX (2021a) Investigation of the fracturing effect induced by the disturbing stress of hydrofracturing using the bonded-particle model. *Geofluids*. <https://doi.org/10.1155/2021/9988748>
- Zhang X, Zhang YQ, Zhang T (2021b) Experimental and numerical investigation on hydraulic fracture propagation law of composite rock materials considering the disturbing stress effect. *Geofluids*. <https://doi.org/10.1155/2021/9920633>
- Zhao ZH, Li X, Wang Yu, Zheng B, Zhang B (2016) A laboratory study of the effects of interbeds on hydraulic fracture propagation in shale formation. *Energies* 9(7):556. <https://doi.org/10.3390/en9070556>
- Zhao HF, Wang XH, Liu ZY, Yan YJ, Yang HX (2018) Investigation on the hydraulic fracture propagation of multilayers-commingled fracturing in coal measures. *J Pet Sci Eng* 167:774–784. <https://doi.org/10.1016/j.petrol.2018.04.028>
- Zhao HF, Wang XH, Wang ZY, Liu B (2019) Experimental investigation of hydraulic sand fracturing on fracture propagation under the influence of coal macrolithotypes in Hancheng block, China. *J Pet Sci Eng* 175:60–71. <https://doi.org/10.1016/j.petrol.2018.12.031>
- Zhao X, Jin F, Liu X, Zhang Z, Cong Z, Li Z, Tang J (2022) Numerical study of fracture dynamics in different shale fabric facies by integrating machine learning and 3-D lattice method: a case from Cangdong Sag, Bohai Bay Basin, China. *J Petrol Sci Eng* 218:110861. <https://doi.org/10.1016/j.petrol.2022.110861>
- Zheng YX, Liu J, Zhang B (2019) An investigation into the effects of weak interfaces on fracture height containment in hydraulic fracturing. *Energies* 12:3245. <https://doi.org/10.3390/en12173245>
- Zhou ZL, Zhang GQ, Dong HR, Liu ZB, Nie YX (2017) Creating a network of hydraulic fractures by cyclic pumping. *Int J Rock Mech Min* 97:52–63. <https://doi.org/10.1016/j.ijrmms.2017.06.009>
- Zhou J, Zeng YJ, Jiang TX, Zhang BP (2018) Laboratory scale research on the impact of stress shadow and natural fractures on fracture geometry during horizontal multi-staged fracturing in shale. *Int J Rock Mech Min* 107:282–287. <https://doi.org/10.1016/j.ijrmms.2018.03.007>
- Zou YS, Ma XF, Zhou T, Li N, Zhang YN, Li SH, Li H, Chen M (2017) Hydraulic fracture growth in a layered formation based on fracturing experiments and discrete element modeling. *Rock Mech Rock Eng* 50:2381–2395. <https://doi.org/10.1007/s00603-017-1241-z>
- Zhuang XY, Zhou SW, Sheng M, Li GS (2020) On the hydraulic fracturing in naturally-layered porous media using the phase field method. *Eng Geol* 266:105306. <https://doi.org/10.1016/j.enggeo.2019.105306>

Publisher's Note Springer Nature remains neutral with regard to jurisdictional claims in published maps and institutional affiliations.

Springer Nature or its licensor holds exclusive rights to this article under a publishing agreement with the author(s) or other rightsholder(s); author self-archiving of the accepted manuscript version of this article is solely governed by the terms of such publishing agreement and applicable law.